

In presenting the dissertation as a partial fulfillment of the requirements for an advanced degree from the Georgia Institute of Technology, I agree that the Library of the Institute shall make it available for inspection and circulation in accordance with its regulations governing materials of this type. I agree that permission to copy from, or to publish from, this dissertation may be granted by the professor under whose direction it was written, or, in his absence, by the Dean of the Graduate Division when such copying or publication is solely for scholarly purposes and does not involve potential financial gain. It is understood that any copying from, or publication of, this dissertation which involves potential financial gain will not be allowed without written permission.

7-1-68

7/25/68

NEUTRON INELASTIC SCATTERING STUDIES
OF THE ISING SYSTEM FeCO_3

A THESIS

Presented to

The Faculty of the Division of Graduate
Studies and Research

by

Douglas Ewart Wrege


In Partial Fulfillment
of the Requirements for the Degree
Doctor of Philosophy
in the School of Physics

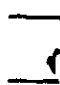
Georgia Institute of Technology

October, 1971

NEUTRON INELASTIC SCATTERING STUDIES
OF THE ISING SYSTEM FeCO_3

Approved:


Chairman


Date approved by Chairman: 1 Nov 1971

ACKNOWLEDGMENTS

The author wishes to express his deepest appreciation to Drs. S. Spooner and H. A. Gersch for their professional guidance and personal encouragement during the course of this work.

The author is grateful for having at his disposal the excellent experimental facilities of the Oak Ridge National Laboratory and the scientific expertise of the members of the Solid State Division. Special appreciation is extended to Dr. M. K. Wilkinson, Associate Director, who served on the reading committee, for the consideration given to the author during this work. The experimental assistance and helpful discussions with Drs. R. M. Nicklow and H. A. Mook are gratefully acknowledged. The author would like to thank Dr. S. W. Lovesay for his invaluable suggestions.

The author would also like to thank Drs. D. P. Landau and D. C. O'Shea for their helpful discussions.

Dr. D. W. Forester is thanked for supplying one of the samples used.

Finally, the author would like to thank his wife for her patience and assistance. Her background in physics has proved invaluable during this endeavor.

This research was supported by U.S. Atomic Energy Commission Contract #AT-(40-1)-3674.

TABLE OF CONTENTS

	Page
ACKNOWLEDGMENTS.	ii
LIST OF TABLES	v
LIST OF ILLUSTRATIONS.	vi
SUMMARY.	viii
Chapter	
I. INTRODUCTION.	1
Magnetic Exchange and the Ising Model	
Character of the Ising Dispersion Curve	
The Spin-Lattice Interaction	
Techniques for Studying Cooperative Modes	
in Solids	
The Specific Problem of FeCO_3 .	
II. THEORY.	10
Crystal Field Theory	
Antiferromagnetic Magnons	
The Spin-Lattice Interaction	
Renormalization of the Spin-Lattice	
Hamiltonian	
III. THE EXPERIMENT.	27
The Equipment	
Alignment of the Sample	
The Interaction of Neutrons with Matter	
Resolution Function Focusing	
Data Collection Method	
Contamination	
The Samples	
IV. RESULTS AND DISCUSSION	44
Presentation of the Data	
The Ising Character of FeCO_3	
The Spin-Lattice Interaction	

TABLE OF CONTENTS (Concluded)

Chapter	Page
V. CONCLUSIONS AND RECOMMENDATIONS	65
Appendices	
A. PRESENTATION OF THE DATA.	69
B. NONLINEAR LEAST SQUARES FITTING	76
C. A COMPUTER CONTROLLED NEUTRON DIFFRACTOMETER AT THE GTRR	79
Design Philosophy	
The Hardware System	
The Software System	
Typical Operation	
BIBLIOGRAPHY	94
VITA	97

LIST OF TABLES

Table	Page
1. Spin-Orbit Splitting Parameters for Fe^{2+} Impurities in Compounds	51
2. Excitations in FeCO_3 Determined by Neutron Inelastic Scattering.	70
3. IOT Instructions for Neutron Diffraction Computer Control.	84

LIST OF ILLUSTRATIONS

Figure	Page
1. Unit Cell of Iron Carbonate	11
2. Crystal Field Splitting of Fe^{2+} in FeCO_3	12
3. Schematic Diagram of the Triple-Axis Spectrometer at the High Flux Isotope Reactor	28
4. Scattering Plane in FeCO_3 Containing the Threefold and the Twofold Axes.	35
5. Resolution Function Focusing Effects in Triple-Axis Neutron Diffractometry.	38
6. Constant-Q and Constant-E Methods of Scan	39
7. Brillouin Zone of FeCO_3 Illustrating High Symmetry Lines and Points	45
8. Phonon Spectra in the High Symmetry Directions in FeCO_3	46
9. Magnetic Excitations Observed in FeCO_3 at 4.2 K.	47
10. Typical Neutron Groups for Longitudinal Scans in the Λ -Direction Near Nominal Crossover	53
11. Typical Neutron Group for Transverse Scan in the Λ -Direction Near Nominal Crossover	55
12. Neutron Groups Observed for Transverse Scans in the Δ -Direction Near Nominal Crossover	56
13. Neutron Groups Observed for Transverse Scans in the Δ -Direction Near Nominal Crossover	57
14. Integrated Intensities of Neutron Groups in the Δ -Direction Indicating the Degree of Magnon Character.	61

LIST OF ILLUSTRATIONS (Concluded)

Figure		Page
15.	Transverse Phonon Dispersion Curve in the Λ -Direction as a Function of Temperature.	63
16.	Phonon Dispersion Relations in FeCO_3 and CaCO_3 in the Λ -Direction.	67
17.	Logic Design for the GTRR Computer Controlled Neutron Diffraction Interface	83
18.	Logic Design and Utilization of the Scalar Timer Interface for the GTRR Computer Controlled Neutron Diffraction Interface, Part I.	85
19.	Logic Design and Utilization of the Scalar Timer Interface for the GTRR Computer Controlled Neutron Diffraction Interface, Part II	86
20.	A Typical FOCAL Program Used for Inelastic Neutron Scattering Experiments.	90
21.	Schematic of the Reciprocal Space Representation of a FOCAL Controlled Inelastic Scan.	92

SUMMARY

The technique of neutron inelastic scattering provides a method of determining the entire energy versus wavevector relationship of cooperative modes in crystals. Neutrons, by virtue of their magnetic moment, provide a unique probe for the microscopic study of magnetic crystals. Since the neutron has no electric charge the magnetic interactions are not masked by coulombic or other long range interactions. This thesis is concerned with the study of the magnetic excitations of a highly anisotropic antiferromagnet, FeCO_3 .

Neutron inelastic scattering measurements were made on single crystals of FeCO_3 at 4.2°K and 300°K , using a triple-axis neutron diffraction technique. The low temperature measurements determined the magnetic excitation dispersion relation for the two high symmetry directions (the threefold and twofold rotation axes). The observed energy relation had no wavevector dependence, within experimental accuracy, which demonstrates that FeCO_3 is accurately described by an Ising model exchange interaction at low temperatures.

Phonon dispersion relations were measured at room temperature along the two high symmetry directions for comparison with the low temperature data. A spin-lattice coupling was observed that removed the degeneracy between the magnetic excitation and certain lattice vibrational modes. The magnetic excitation was observed to couple only to the degenerate transverse phonon branch in the trigonal direction and to one of the two

transverse phonon branches in the twofold direction. The coupling strength of this interaction was comparable to the exchange interaction. This symmetry dependent magnon-phonon coupling is explained in terms of a lattice perturbation on the crystal field splitting of the orbital states of the Fe^{2+} ion. This perturbation is coupled to the spin through the spin-orbit interaction. The resulting spin-lattice Hamiltonian, linear in magnon and phonon operator cross terms, was in quantitative agreement with the observed intensities of the renormalized excitations.

CHAPTER I

INTRODUCTION

Research in the field of magnetism in solids has received considerable attention because of its interest as a fundamental phenomenon in the study of the solid state and because of its importance in the area of technical applications. Since magnetic phenomena are a result of interaction between moving electrons, theories of magnetism are primarily based on models of electronic structure. Although basic questions remain, the subject has been remarkably well served by models including the simple molecular-field theory and the more sophisticated Heisenberg and Stoner theories of magnetism.

A general first-principles theory of magnetism in solids is very difficult because of the necessity of considering the magnetic electrons as only partially localized, with a mixture of itinerant character. An essential simplification results for those special solids where the electrons giving rise to magnetic properties can be adequately considered as completely localized. These are just the assumptions that are made in describing magnetic insulators. The insulator system studied in this work, FeCO_3 , was chosen because of certain simplifications which appear to apply. In particular, this study began with the objective of investigating the degree to which iron carbonate could be described by the Ising model, the simplest of all microscopic descriptions of electronic interactions in magnetic materials.

The Ising nature of the magnetic structure of iron carbonate is a result of the crystal field-splitting of the Fe^{2+} ion. This splitting gives rise to the highly anisotropic result $\langle L_z \rangle = \pm 1$, $\langle L_x \rangle = \langle L_y \rangle = 0$, to be discussed later. Ordinarily magnetocrystalline anisotropy results in $\langle L_z \rangle \neq \langle L_x \rangle \neq \langle L_y \rangle$, but none of these vanish. For this case one must use an anisotropic Heisenberg model which is very complicated. In iron carbonate uniaxial anisotropy is sufficiently strong that the spins are locked along the anisotropy axis, hence the effective magnetic coupling exists only between the component of the spins along that axis. Thus for iron carbonate, anisotropy actually results in a simplification of the quantum mechanical description.

Quantitative calculations in many body theory are dependent on a known ground state. For the antiferromagnet, such as FeCO_3 , the ground state of the crystal is described in terms of two interpenetrating sublattices where the nearest neighbors from one sublattice all lie on the other sublattice. The magnetic moments of all ions on a sublattice are parallel and the moments on the two sublattices are antiparallel to each other. This state is not a stationary state in the Heisenberg model as a consequence of torques on the spin system resulting from the $S^x S^x$ and $S^y S^y$ interactions; hence, the ground state for this model is not precisely known. However, for the Ising model the antiferromagnetic state is a stationary state since there are no x-x or y-y interactions of the spins. The Ising model ground state is well known.

It is apparent from the above that theoretical analysis of a physical system approximating the Ising model is greatly simplified. An

additional benefit of such simplification is that it is possible to observe effects from higher order terms in the Hamiltonian which would normally be obscured. It is shown that iron carbonate is a system of sufficient simplicity to allow study of spin-lattice interaction effects.

Magnetic Exchange and the Ising Model

For insulators the magnetic electrons may be considered to be localized on lattice sites and for critical temperatures exceeding 20°K, electromagnetic dipolar interactions may usually be neglected.¹ These assumptions lead to a magnetic Hamiltonian of the form

$$H = -2 \sum_{ij} J(\vec{r}_i - \vec{r}_j) \vec{S}_i \cdot \vec{S}_j \quad (1)$$

known as the Heisenberg Hamiltonian. The exchange integral J is positive for ferromagnetic coupling and negative for antiferromagnetic ordering. The operators \vec{S}_i and \vec{S}_j are the spin angular momenta for the electrons on the i^{th} and j^{th} lattice sites.

We may rewrite Equation (1) to account for anisotropic exchange as,

$$H = -2 \sum_{ij} \left\{ J_{\parallel}(\vec{r}_i - \vec{r}_j) S_i^z S_j^z + J_{\perp}(\vec{r}_i - \vec{r}_j) (S_i^x S_j^x + S_i^y S_j^y) \right\} . \quad (2)$$

The pure isotropic Heisenberg magnet would correspond to $J_{\parallel} = J_{\perp}$, and for systems with simple uniaxial anisotropy $J_{\parallel} > J_{\perp}$. Theoretically Equation (2) is difficult to work with since the operators in the Hamiltonian do not commute. In the extreme anisotropic limit, $J_{\perp} = 0$, the system corresponds to the Ising model and all operators in the Hamiltonian commute.

The Hamiltonian for the Ising model is thus,

$$H = -2 \sum_{i,j} J(\vec{r}_i - \vec{r}_j) S_i^z S_j^z . \quad (3)$$

Hence S_i^z is a constant of the motion and the system effectively obeys classical mechanics.

As a result of these theoretical simplifications the Ising model has been thoroughly studied. Thermodynamic investigations have been made for specific lattices in one, two, and three dimensions, including exact analytic solutions for the one-dimensional and some two-dimensional lattices.

Until recently, the primary application of the Ising model to magnetic systems provided simple theoretical tests of the validity of various approximations to more physically realistic models and to make possible approximate calculations which could not be accomplished in more complicated systems. Recently a number of systems have been investigated²⁻¹⁷ which appear to be Ising-like to varying degrees in one, two, or three dimensions. Unfortunately the majority of these systems have a complicated crystal structure, a low critical temperature, or a long range interaction in certain symmetry directions; therefore, comparison of experiment and theory is difficult. A notable exception to these complicating factors is FeCO_3 , the subject of this work. The discovery of Ising systems in nature affords the possibility of making additional progress in the theoretical characterization of magnetic phenomena.

Character of the Ising Dispersion Curve

Since the individual spin operators S_i^z in Equation (3) commute with the Hamiltonian, each spin S_i^z is a constant of the motion. Thus, the dynamics in the spin system usually associated with the term magnon or spin-wave is absent and the fundamental excitation is a stationary spin-flip. The energy ϵ of the magnetic excitation is independent of momentum transfer \vec{q} ; consequently, the dispersion curve $\epsilon(\vec{q})$ is flat. The \vec{q} -dependence observed in a dispersion curve is a sensitive measure of the degree of Ising character of a magnetic system.

The Spin-Lattice Interaction

The spin-lattice interaction is an important relaxation mechanism for a magnetic system. Excluding phenomenological theories, the most popular magnon-phonon interaction model assumes that the Ising spins are tightly bound to the ions of a lattice and that the spins interact via an exchange interaction which may be expanded to first order in the ionic displacements (assumed harmonic). This type of treatment results in terms in the Hamiltonian which are linear in the phonon operators and quadratic in the magnon operators.^{18,19} To first order,

$$H = -2 \sum_{i,j} \left\{ J(\vec{R}_i - \vec{R}_j) + (\vec{u}_i - \vec{u}_j) \cdot \vec{\nabla} J(\vec{r}_i - \vec{r}_j) \Big|_R \right\} S_i^z S_j^z . \quad (4)$$

The term $(\vec{u}_i - \vec{u}_j)$ may be expanded into a linear sum of phonon creation and destruction operators and $S_i^z S_j^z$ will result in even products of magnon creation and destruction operators. The salient feature of this perturbation expansion is that the resulting magnon-phonon coupling term will

be finite for all phonon modes provided that the separation of the magnetic ions is modulated by the ion motions. It would be extremely unlikely that this coupling would be dependent on the group symmetry of the lattice vibration.

A second model is based on a lattice vibrational perturbation of the crystal field which perturbs the orbital state of the magnetic ion. This perturbation then couples to the spin system through the spin-orbit interaction. This type of perturbation scheme leads to terms that are linear in both magnon and phonon operators.²⁰ In addition, as crystal symmetry plays an important role in crystal field effects, it is entirely plausible that only phonon modes with a particular symmetry will couple to the magnetic excitations. Therefore, qualitative observations of symmetry dependence of the spin-lattice interaction provide a basis of selection between models that are applicable.

Techniques for Studying Cooperative Modes in Solids

Dispersion relations reveal in the most direct way the details of interactions giving cooperative modes in solids. The energy necessary to excite a magnon, for example, is a simple function of the interaction constants and the momentum transfer at low temperatures (where the system is in its ground state). Interpretation of this type of investigation requires no theoretical models or approximations beyond the well established spin-wave theory. The interpretations of measurements such as specific heat, magnetic susceptibility, and bulk magnetization can be rather indirect and are consequently subject to the use of complex assumptions.

The techniques used for measurement of dispersion relations are

infrared absorption and Raman scattering of light, acoustic determination of elastic constants, x-ray diffraction, and neutron diffraction. Optical infrared and Raman first order processes give information about polar and symmetric modes, respectively, as well as information on the magnetic excitations at the Brillouin zone center. Second order processes reveal information away from the zone center; however, the spectra are sufficiently complex to make interpretation difficult without some prior knowledge of the phenomena under study. Velocity-of-sound measurements provide data to determine elastic constants from which the slope of phonon dispersion curves at zero wavevector may be determined, but information about magnetic dispersion cannot be determined by acoustic methods. X-ray diffuse scattering may be used; however, extremely careful intensity measurements are required and interpretation is difficult. As in the above methods, information about the magnetic dispersion cannot be obtained from x-ray experiments.

Inelastic scattering of thermal neutrons is ideally suited for the determination of complete energy versus wavevector spectrum. Energies of thermal neutrons are of the same order as the typical energies involved in spin-wave or phonon creation, so energy changes produced by these excitations are easily measured. The momentum transfer is directly measured by the change in the direction of the flight of the scattered neutron. Thus, the dispersion relation of the cooperative phenomena may be determined for the entire wavevector spectrum of that excitation. The most significant advantage of neutron scattering is in the area of investigations of magnetic phenomena. Since the neutron possesses a magnetic moment

but no electric charge, there is an interaction with magnetic electrons in the crystal which is not masked by stronger interactions arising from coulombic forces. In effect, only those electrons which contribute to the magnetic properties of the system interact with the neutron.

The Specific Problem of FeCO_3

Iron carbonate has a rhombohedral structure belonging to the space group D_{3d}^6 ($R\bar{3}c$) and has high symmetry (see Figure 1) compared to other postulated Ising systems. The Fe^{2+} ions order antiferromagnetically near 38°K in alternating (001) ferromagnetic sheets with the spins locked along the trigonal (c) axis. This antiferromagnetic structure has been established by magnetic susceptibility^{21,22} and neutron diffraction²³ measurements. It has been demonstrated^{24,25} that the moments even remain bound to the trigonal axis for temperatures well into the paramagnetic region.

One of the characteristics of FeCO_3 (the mineral siderite) is that it undergoes a transition from antiferromagnetic to ferromagnetic order in high magnetic fields at low temperatures.²⁶ This phenomena, termed metamagnetism, occurs in contrast to the more normally found spin-flop transition (in which the ordering remains antiferromagnetic but the magnetization direction shifts to a direction perpendicular to the applied field). Metamagnetism is explained on the basis that the anisotropy is sufficiently high so that the exchange energy is exceeded before the anisotropy energy. Thus, it seems reasonable to regard this type of system as an Ising-model system with only S^z - S^z interactions. A microscopic theory has been developed by Kanamori^{27,28} which demonstrates that the Ising model is applicable to FeCO_3 at low temperatures, with a large

anisotropy energy directing the spins parallel to the trigonal axis.

Summarizing, iron carbonate appears to be a physical realization of a three-dimensional Ising model with relatively high symmetry. The purpose of this research was:

1. to establish the degree of Ising character of the system through determination of the dispersion curve for the magnetic excitations, and
2. to establish the exact nature of the spin-lattice interaction, i.e. whether the interaction is a result of modulation of the exchange integral or if the coupling appears to act through the crystal field.

CHAPTER II

THEORY

Crystal Field Theory

The Ising character of iron carbonate was theoretically postulated by Kanamori²⁷ while discussing FeCl_2 . Later Okiji and Kanamori²⁸ extended this crystal field theoretical study to FeCO_3 . Recently this theory has been successful in the interpretation of Mössbauer studies by Koon²⁴ and Ok²⁵. Since an understanding of their work is important for subsequent interpretations, this section is devoted to a brief outline of their results as they apply to iron carbonate.

The ground state of the free Fe^{2+} ion has a $^5\text{D}_4$ electronic configuration, $L = S = 2$. Since the carbonate ions form a body-centered cubic lattice with trigonal distortion, Figure 1, the major portion of the crystalline field about the Fe^{2+} ion has cubic symmetry. In this field the fivefold degenerate ground orbital splits into a doublet and a triplet separated by typically $10,000 \text{ cm}^{-1}$ (Figure 2). Application of a trigonal field, resulting from distortion into a rhombohedron, splits this triplet into a singlet and a doublet, separated by approximately 1000 cm^{-1} . It is assumed that the doublet is the lowest orbital state, as the anisotropy energy favoring the trigonal axis cannot be obtained otherwise.²⁷

If the trigonal axis is defined as the axis of quantization, the orbital doublet may be written,²⁸

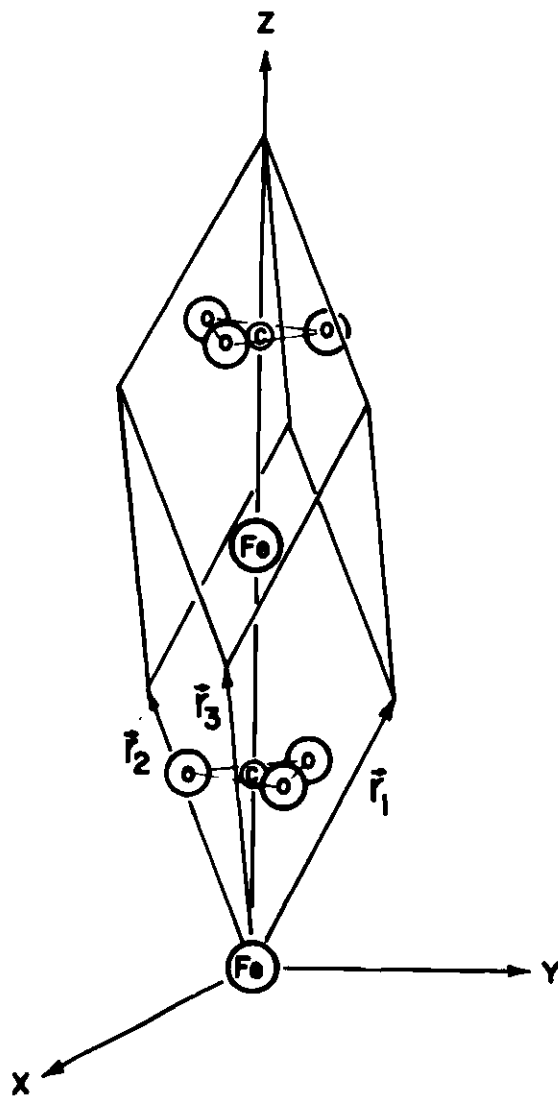


Figure 1. Unit Cell of Iron Carbonate

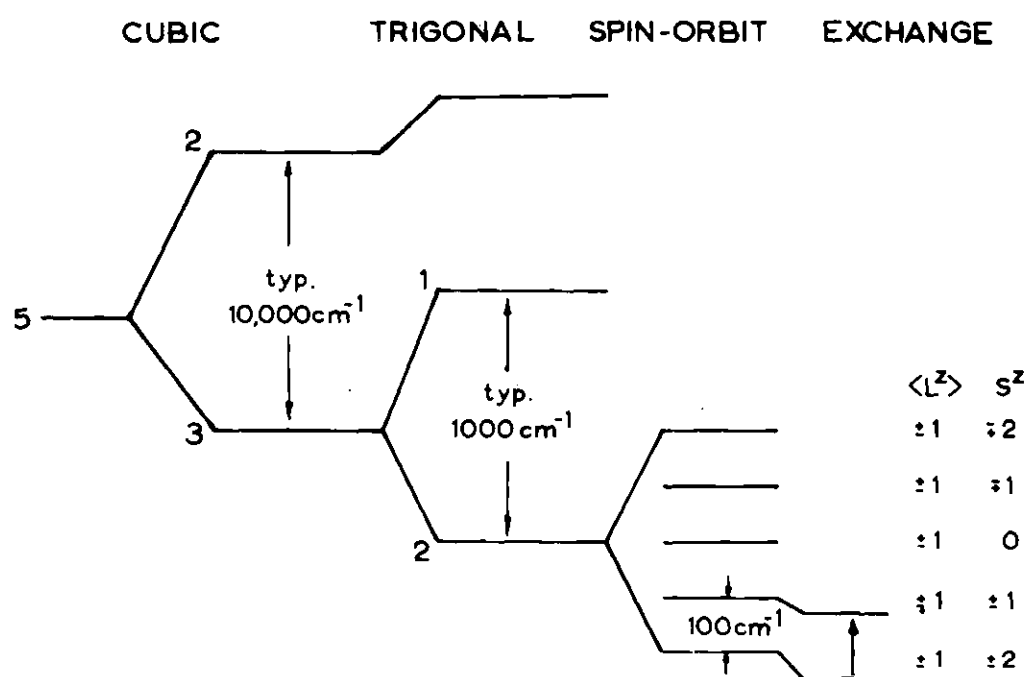


Figure 2. Crystal Field Splitting of Fe^{2+} in FeCO_3

$$|g1\rangle = \cos\theta |L=2, m_L=2\rangle + \sin\theta |2, -1\rangle \quad (5)$$

$$|g2\rangle = \cos\theta |2, -2\rangle - \sin\theta |2, 1\rangle$$

where $|L, m_L\rangle$ are orbital wave functions and θ is a mixing parameter to be experimentally determined.*

The orbital wave function of the singlet is

$$|s\rangle = |2, 0\rangle \quad (6)$$

and the upper doublet is

$$|h1\rangle = \sin\theta |2, 2\rangle - \cos\theta |2, -1\rangle \quad (7)$$

$$|h2\rangle = \sin\theta |2, -2\rangle + \cos\theta |2, 1\rangle .$$

It can easily be shown with these wave functions that in the ground doublet L^z is diagonal with

$$\langle g1 | L^z | g1 \rangle = - \langle g2 | L^z | g2 \rangle = \frac{1 + 3\cos(2\theta)}{2} \approx 1.1 \quad (8)$$

and all matrix elements of L^x and L^y vanish.

Introducing the Pauli σ_z^L matrix operating on the two dimensional space spanned by $|g1\rangle$ and $|g2\rangle$, we may write the spin orbit energy to first order as,

* $\cos\theta \approx 0.838$ as estimated by Okiji and Kanamori.²⁸

$$\lambda < L > \sigma_z^L S^z, \quad (9)$$

where $< L > \equiv < g1 | L^z | g1 >$.

Thus the ground orbital doublet (each with fivefold spin degeneracy) is split into five equally spaced doublets, specified by

$$\sigma_z^L = 1, S^z = m \quad \text{and} \quad \sigma_z^L = -1, S^z = -m \quad (m = 2, \dots, -2) \quad (10)$$

the spacing is $|\lambda| < L >$ with the lowest doublet $\sigma_z^L = 1, S^z = 2$ and $\sigma_z^L = -1, S^z = -2$. Assuming $< L > = 1$, cubic symmetry, and the free ion value of $\lambda = -100 \text{ cm}^{-1}$, the doublets will be spaced by approximately $|\lambda| < L > = 100 \text{ cm}^{-1}$. Therefore below the Néel temperature, 38°K , only the lowest doublet will be populated. In the space spanned by this ground state doublet S^x, S^y, L^x , and L^y have zero matrix elements. Consider the exchange Hamiltonian representing the interaction between Fe^{2+} ions, which in general has the Heisenberg form given by Equation (1). Below 38°K we may retain only the diagonal part of this Hamiltonian with respect to the ground state doublet, and write

$$H_{\text{ex}} = -2 \sum_{ij} J_{ij} S_i^z S_j^z. \quad (11)$$

Antiferromagnetic Magnons

There is no propagation of a spin deviation in an Ising system. Therefore, the term spin-wave or magnon is a misnomer, so one should use less ambiguous terms like exciton or simply magnetic excitation. However,

keeping this in mind, we shall use all of the above terms when describing magnetic excitations in this work.

Following Kittel,²⁹ we divide the spin structure of the lattice into two interpenetrating sublattices, labeled a and b, where nearest neighbors of the a lattice all lie on the b lattice and vice versa. Consider the Heisenberg Hamiltonian

$$H = -2J \sum_{j\delta} \vec{S}_j \cdot \vec{S}_{j+\delta} - 2\mu_o H_A \sum_j S_{jz}^a + 2\mu_o H_A \sum_j S_{jz}^b, \quad (12)$$

where we have assumed nearest neighbor interactions. J is the exchange integral, δ is a sum over neighbors, and H_A is the anisotropy field. The derivation will be carried out for both the Heisenberg and Ising systems so that the differences may be made apparent.

The Holstein-Primakoff transformation to boson creation and destruction operators, a, a^\dagger for the a sublattice is defined by:

$$S_{aj}^+ = S_{aj}^x + iS_{aj}^y = (2S)^{1/2} (1 - a_j^\dagger a_j / 2S)^{1/2} a_j, \quad (13)$$

$$S_{aj}^- = S_{aj}^x - iS_{aj}^y = (2S)^{1/2} a_j^\dagger (1 - a_j^\dagger a_j / 2S)^{1/2}$$

while for the b sublattice, the transformation is to boson operators b, b^\dagger

$$S_{bl}^+ = S_{bl}^x - iS_{bl}^y = (2S)^{1/2} b_l^\dagger (1 - b_l^\dagger b_l / 2S)^{1/2}, \quad (14)$$

$$S_{bl}^- = S_{bl}^x + iS_{bl}^y = (2S)^{1/2} (1 - b_l^\dagger b_l / 2S)^{1/2} b_l.$$

In order that S^+ and S^- satisfy correct commutation relations the operators a , a^\dagger , b , and b^\dagger must satisfy

$$[a_j, a_k^\dagger] = \delta_{j,k} \quad \text{and} \quad [b_j, b_k^\dagger] = \delta_{j,k} . \quad (15)$$

The motivation for defining S_{b1}^+ similar to S_{aj}^- is that a raising operator on the b sublattice (increasing the component in the minus z -direction) is equivalent to a lowering operator on the a sublattice. The operators a_j^\dagger and a_j are spin operators which create and destroy unit spin at the j^{th} site of sublattice a ; they are not magnon operators.

From Equations (13) and (14),

$$\begin{aligned} S_{az}^2 &= S(S+1) - S_{ax}^2 - S_{ay}^2 \\ &= S(S+1) - (S_a^+ S_a^- + S_a^- S_a^+)/2 \\ &= (S - a^\dagger_a)^2 . \end{aligned}$$

Similarly,

$$S_{bz}^2 = (S - b^\dagger_b)^2 .$$

We may thus write

$$S_{aj}^z = S - a_j^\dagger a_j \quad \text{and} \quad S_{b1}^z = -S + b_1^\dagger b_1 , \quad (16)$$

where the choice of sign for the two sublattices is to maintain similarity in definitions of a^\dagger and b^\dagger between the two sublattices.

At this point we have proceeded as far as is physically meaningful for the case of the Ising system. The Hamiltonian is diagonalized in the number space of the spin deviation operators, $a_j^\dagger a_j = n_{aj}$ and $b_l^\dagger b_l = n_{bl}$, where n_{aj} is the number operator for spin deviations on the a sublattice. We would have

$$H_{\text{Ising}} = 4NzJS^2 - 4N\mu_o H_A S - 2JzS \sum_j (n_{aj} + n_{bj}) \quad (17)$$

$$+ 2\mu_o H_A \sum_j (n_{aj} + n_{bj}) + 2J \sum_{j\delta} (n_{aj} n_{b,j+\delta} + n_{bj} n_{a,j+\delta})$$

where N is the number of magnetic ions on each sublattice and the last term in $N_a n_b + n_b n_a$ would normally be dropped as a higher order term. However, one can always introduce the normal spin wave variables

$$c_k = N^{-1/2} \sum_j e^{i\vec{k} \cdot \vec{x}_j} a_j ; \quad c_k^\dagger = N^{-1/2} \sum_j e^{-i\vec{k} \cdot \vec{x}_j} a_j^\dagger , \quad (18)$$

$$d_k = N^{-1/2} \sum_l e^{-i\vec{k} \cdot \vec{x}_l} b_l ; \quad d_k^\dagger = N^{-1/2} \sum_l e^{i\vec{k} \cdot \vec{x}_l} b_l^\dagger ,$$

where the j sum is over sublattice a and the l sum is over the b sublattice. Hence the c 's operate on the a sublattice and the d 's on the b sublattice. In terms of these operators, Equations (13) and (14) become (displaying only lowest order terms)

$$S_{aj}^+ = (2S/N)^{1/2} \sum_k e^{-i\vec{k} \cdot \vec{x}_j} c_k + \dots \quad (19)$$

$$S_{aj}^- = (2S/N)^{1/2} \sum_k e^{i\vec{k} \cdot \vec{x}_j} c_k^\dagger + \dots$$

$$S_{b1}^+ = (2S/N)^{1/2} \sum_k e^{-i\vec{k} \cdot \vec{x}_1} d_k^\dagger + \dots$$

$$S_{b1}^- = (2S/N)^{1/2} \sum_k e^{i\vec{k} \cdot \vec{x}_1} d_k + \dots ,$$

and Equation (16) becomes

$$S_{aj}^z = S - (1/N) \sum_{kk'} e^{i(\vec{k}-\vec{k}') \cdot \vec{x}_j} c_k^\dagger c_{k'}, \quad (20)$$

$$S_{b1}^z = S - (1/N) \sum_{kk'} e^{-i(\vec{k}-\vec{k}') \cdot \vec{x}_1} d_k^\dagger d_{k'} .$$

We define the magnetic Hamiltonian

$$H = H_A + H_I + H_H, \quad (21)$$

where H_A is the crystalline anisotropy term, H_I is the Ising exchange, and H_H , contains the additions necessary for the Heisenberg model. The anisotropy term is

$$H_A = -4N\mu_o H_A S + 2\mu_o H_A \sum_k (c_k^\dagger c_k + d_k^\dagger d_k) , \quad (22)$$

and the Ising term for z nearest neighbors is

$$\begin{aligned}
H_I &= - 2J \sum_{j\delta} S_j^z S_{j+\delta}^z \\
&= - 2J \sum_{j\delta} S_{aj}^z S_{b,j+\delta}^z + \sum_{1\delta}^b S_{b1}^z S_{a,1+\delta}^z \\
&= 4NzJS^2 - 2JzS \sum_k (c_k^\dagger c_k + d_k^\dagger d_k) .
\end{aligned} \tag{23}$$

The additional terms are the difference between the Ising and Heisenberg models:

$$\begin{aligned}
H_H &= - 2J \sum_{j\delta} (S_j^x S_{j+\delta}^x + S_j^y S_{j+\delta}^y) \\
&= - 2JzS \sum_k \gamma_k (c_k^\dagger d_k + c_k^\dagger d_k) + \dots ,
\end{aligned} \tag{24}$$

where $\gamma_k = (1/z) \sum_{\delta} e^{i\vec{k} \cdot \vec{\delta}}$. We shall neglect all high order terms at this point and note that we may reduce H to the Ising case at any of the following steps by setting $\gamma_k = 0$.

A transformation that diagonalizes H^{29} is

$$\begin{aligned}
\alpha_k &= u_k c_k - v_k d_k^\dagger , & \alpha_k &= u_k c_k^\dagger - v_k d_k , \\
\beta_k &= u_k d_k - v_k c_k^\dagger , & \beta_k &= u_k d_k^\dagger - v_k c_k ,
\end{aligned} \tag{25}$$

where

$$\begin{aligned}
[\alpha_k, \alpha_k^\dagger] &= 1 , \\
[\beta_k, \beta_k^\dagger] &= 1 ,
\end{aligned} \tag{26}$$

(Continued)

$$[\alpha_k, \beta_k] = 0 ,$$

$$u_k^2 - v_k^2 = 1 \quad \text{with } u_k, v_k \text{ real.}$$

Hence,

$$c_k = u_k \alpha_k - v_k \beta_k^\dagger \quad \text{and} \quad d_k = u_k \beta_k - v_k \alpha_k^\dagger . \quad (27)$$

Writing

$$\omega_0 = -2JzS + 2\mu_0 H_A$$

$$\omega_1 = -2JzS\gamma_k ,$$

the terms bilinear in magnon variables, designated by H' ,

$$H' = \omega_0 \sum_k (c_k^\dagger c_k + d_k^\dagger d_k) + \omega_1 \sum_k (c_k^\dagger d_k^\dagger + c_k d_k) \quad (28)$$

become

$$\begin{aligned} H' = \omega_0 \sum_k \{ & u_k^2 \alpha_k^\dagger \alpha_k + v_k^2 \beta_k \beta_k^\dagger + u_k v_k (\alpha_k^\dagger \beta_k^\dagger + \beta_k \alpha_k) \\ & + u_k^2 \beta_k^\dagger \beta_k + v_k^2 \alpha_k \alpha_k^\dagger + u_k v_k (\beta_k^\dagger \alpha_k^\dagger + \alpha_k \beta_k) \} \\ & + \omega_1 \sum_k \{ u_k v_k (\alpha_k^\dagger \alpha_k + \beta_k \beta_k^\dagger) + u_k^2 \alpha_k^\dagger \beta_k^\dagger + v_k^2 \beta_k \alpha_k \\ & + u_k v_k (\alpha_k \alpha_k^\dagger + \beta_k \beta_k^\dagger) + u_k^2 \alpha_k \beta_k + v_k^2 \beta_k^\dagger \alpha_k^\dagger \} . \end{aligned} \quad (29)$$

The cross terms are

$$\begin{aligned} \text{cross} = & [2\omega_0 u_k v_k + \omega_1 (u_k^2 + v_k^2)] \alpha_k^\dagger \beta_k^\dagger \\ & + [2\omega_0 u_k v_k + \omega_1 (u_k^2 + v_k^2)] \alpha_k \beta_k . \end{aligned}$$

Hence we require that

$$2\omega_0 u_k v_k + \omega_1 (u_k^2 + v_k^2) = 0 . \quad (30)$$

The solution is

$$u_k^2 = \left[-1 + \sqrt{\omega_0^2 / (\omega_0^2 - \omega_1^2)} \right] / 2 \quad (31)$$

$$v_k^2 = \left[1 + \sqrt{\omega_0^2 / (\omega_0^2 - \omega_1^2)} \right] / 2$$

giving

$$H' = \sum_k \left\{ \omega_k (\alpha_k^\dagger \alpha_k + \beta_k^\dagger \beta_k + 1) \right\} - N\omega_0 , \quad (32)$$

where $\omega_k^2 = \omega_0^2 - \omega_1^2$. The complete Hamiltonian is now

$$H = -4N\mu_0 H_A S + 4NzJS^2 + 2NJzS - 2N\mu_0 H_A + \sum_k \left\{ [(-2JzS + \mu_0 H_A)^2 - (2JzS\gamma_k)^2]^{1/2} (\alpha_k^\dagger \alpha_k + \beta_k^\dagger \beta_k + 1) \right\} . \quad (33)$$

The magnon frequencies ω_k are given by

$$\omega_k^2 = (-2JzS + 2\mu_0 H_A)^2 - (2JzS\gamma_k)^2 . \quad (34)$$

Momentum dependence (dispersion) enters only through γ_k . Therefore, for an Ising system ($\gamma_k = 0$), the momentum-energy curve should exhibit no dispersion. This is a consequence of S^z being a constant of the motion since

$$[S^z, H] = 0$$

for the Ising case.

The Spin-Lattice Interaction

We give here a brief description of the spin-lattice interaction which is subsequently treated by a coupling term linear in magnon and phonon operators.

The total Hamiltonian for the FeCO_3 lattice is taken to be

$$H = H_l + H_i + H_{\text{ex}} + V_c + H_{\text{so}} \quad (35)$$

where H_l is the lattice Hamiltonian, describing the vibrations of the atoms in the crystal, and contains only lattice displacement coordinates. H_i describes the bare Fe^{2+} ion, and contains the electron coordinates of the single 3d electron outside of the half filled spherically symmetric 3d shell. H_{ex} is the exchange Hamiltonian describing the interaction between neighboring Fe^{2+} ions. V_c is the electrostatic potential, or crystal field, produced at the Fe^{2+} site by its CO_3 neighbors. The static part of V_c , denoted by V_o , has already been treated in splitting the five-fold degenerate ground state orbital of the Fe^{2+} ion. In addition to the static or rigid ion part V_o , V_c also contains a contribution V_d from the displaced CO_3 ions:

$$V_c = V_o + V_d \quad (36)$$

$$V_d = e^2 \sum_{\delta} (\vec{u}_o - \vec{u}_{\delta}) \cdot \vec{\nabla} \frac{1}{|\vec{r} - \vec{R}_{\delta}|}$$

where $\vec{u}_o - \vec{u}_{\delta}$ is the difference in displacement between the ion at the

origin and its neighbors at distance R_δ . This term is linear in phonon creation and destruction operators. The coordinate \underline{r} refers to the 3d electron on the Fe^{2+} ion which is at the origin.

The term H_{so} is the spin orbit energy,

$$H_{so} = \lambda \mathbf{L} \cdot \mathbf{S} . \quad (37)$$

It is the combined effect of V_d and H_{so} which provides the spin-lattice interaction. These terms are treated as a perturbation acting on the static crystal-field-split states described earlier in this chapter. In first order perturbation theory, H_{so} splits the ground state doublet into five equally spaced doublets, as previously described. The first order contribution from V_d is of no interest to us, since these terms are independent of spin.

In second order perturbation theory, we consider terms of the form $(H_{so} + V_d)^2$, which couple spin and lattice through cross terms $\sim H_{so} V_d$. Such terms will be linear in spin operators, and there is a general theorem that all such terms must vanish.³⁰ In third order perturbation theory, one gets non-zero contribution terms of the form $H_{so}^2 V_d$, and detailed considerations show that they result in terms involving spin operators in the form $S^z S^+$ and $S^z S^-$. Since we consider the Fe^{2+} ion in the ordered state, $S^z \approx S$, so that we get a Hamiltonian linear in phonon operators (linear in V_d) and linear in the operators S^+ and S^- , which are magnon creation and destruction operators.

Renormalization of the Spin-Lattice Hamiltonian

Using a spin-lattice Hamiltonian with linear coupling terms:

$$H_{sl} = \sum_k \left\{ \omega_k^M a_k^\dagger a_k + \omega_k^P b_k^\dagger b_k + c_k (a_k^\dagger b_k + a_k b_k^\dagger) \right\}, \quad (38)$$

where c_k is the coupling constant for the magnon-phonon interaction, a^\dagger and a are magnon creation and destruction operators, b^\dagger and b are phonon creation and destruction operators, ω_k^M is the unperturbed magnon dispersion relation, and ω_k^P is the unperturbed phonon dispersion relation. The creation and destruction operators satisfy the commutation relations for bosons:

$$\begin{aligned} [a_k, a_l^\dagger] &= \delta_{kl} & [a_k, b_l] &= 0 \\ [b_k, b_l^\dagger] &= \delta_{kl} & [a_k, b_l^\dagger] &= 0. \end{aligned} \quad (39)$$

We will transform these excitations into dressed excitations which transform the Hamiltonian into diagonal form.

Let

$$\begin{aligned} a_k &= A_k \cos \theta_k + B_k \sin \theta_k \\ b_k &= B_k \cos \theta_k - A_k \sin \theta_k \end{aligned} \quad (40)$$

where we require that the dressed (renormalized) creation operators satisfy

$$\begin{aligned} [A_k, A_l^\dagger] &= \delta_{kl} & [A_k, B_l] &= 0 \\ [B_k, B_l^\dagger] &= \delta_{kl} & [A_k, B_l^\dagger] &= 0. \end{aligned} \quad (41)$$

The form of the combinations in Equation (40) was chosen to guarantee satisfaction of Equations (41) as a result of Equations (39). Expanding the Hamiltonian in the new operators A_k and B_k

$$\begin{aligned}
 H_{sl} = \sum_k & \left[A_k^\dagger A_k \{ \omega_k^M \cos^2 \theta_k + \omega_k^P \sin^2 \theta_k - 2c_k \sin \theta_k \cos \theta_k \} \right. \\
 & + B_k^\dagger B_k \{ \omega_k^M \sin^2 \theta_k + \omega_k^P \cos^2 \theta_k + 2c_k \sin \theta_k \cos \theta_k \} \\
 & + A_k^\dagger B_k \{ \omega_k^M \cos \theta_k \sin \theta_k - \omega_k^P \cos \theta_k \sin \theta_k + c_k (\cos^2 \theta_k - \sin^2 \theta_k) \} \\
 & \left. + B_k^\dagger A_k \{ \omega_k^M \cos \theta_k \sin \theta_k - \omega_k^P \cos \theta_k \sin \theta_k + c_k (\cos^2 \theta_k - \sin^2 \theta_k) \} \right] .
 \end{aligned} \tag{42}$$

The Hamiltonian will be diagonal in the new operators for θ_k satisfying

$$\begin{aligned}
 (\omega_k^M - \omega_k^P) \cos \theta_k \sin \theta_k + c_k (\cos^2 \theta_k - \sin^2 \theta_k) &= 0 \\
 = (\omega_k^M - \omega_k^P) \frac{1}{2} \sin 2\theta_k + c_k \cos 2\theta_k .
 \end{aligned} \tag{43}$$

The new Hamiltonian is

$$H_{sl} = \sum_k \{ \omega_k^A A_k^\dagger A_k + \omega_k^B B_k^\dagger B_k \} , \tag{44}$$

where the renormalized excitation energies are

$$\begin{aligned}
 \omega_k^A &= \omega_k^M \cos^2 \theta_k + \omega_k^P \sin^2 \theta_k - 2c_k \sin \theta_k \cos \theta_k \\
 \omega_k^B &= \omega_k^M \sin^2 \theta_k + \omega_k^P \cos^2 \theta_k + 2c_k \sin \theta_k \cos \theta_k ,
 \end{aligned} \tag{45}$$

and the θ_k satisfy

$$\tan 2\theta_k = 2c_k / (\omega_k^P - \omega_k^M) . \quad (46)$$

Physically, these new excitations may be considered as a phonon surrounded by a cloud of virtual magnons and a magnon dragging along virtual phonons. Of course, the amount of magnon or phonon character is a function of wavevector: mode A_k being magnon-like for small wavevector and phonon-like for large wavevector.

CHAPTER III

THE EXPERIMENT

The Equipment

The data were collected at the Oak Ridge Research Reactor (ORR) and the High Flux Isotope Reactor (HFIR) at the Oak Ridge National Laboratory. Preliminary elastic and inelastic scattering experiments were conducted at the Georgia Tech Research Reactor (GTRR).^{*} At all installations the inelastic data were collected using triple-axis diffractometry.³¹

A typical triple-axis spectrometer is illustrated schematically in Figure 3.³² A polychromatic beam of neutrons having a thermal spectrum is incident upon a monochromating crystal which Bragg diffracts (elastic reflection) those neutrons with a specific energy E_0 (wavevector \vec{k}_0), determined by $2\theta_M$. This monoenergetic beam passes through a Soller slit collimator to the sample position. The crystal is set at an angle ψ with respect to the beam to obtain the desired orientation of reciprocal space. The neutrons which are scattered through an angle ϕ pass through a pre-analyzer collimator to the analyzer which is set ($2\theta_A$) to Bragg reflect neutrons of a particular energy E_1 (wavevector \vec{k}_1) into the detector.

^{*}The computer control for a triple axis spectrometer was designed and constructed by the author to facilitate preliminary experiments and training in inelastic neutron diffractometry. A description of this facility is given in Appendix C.

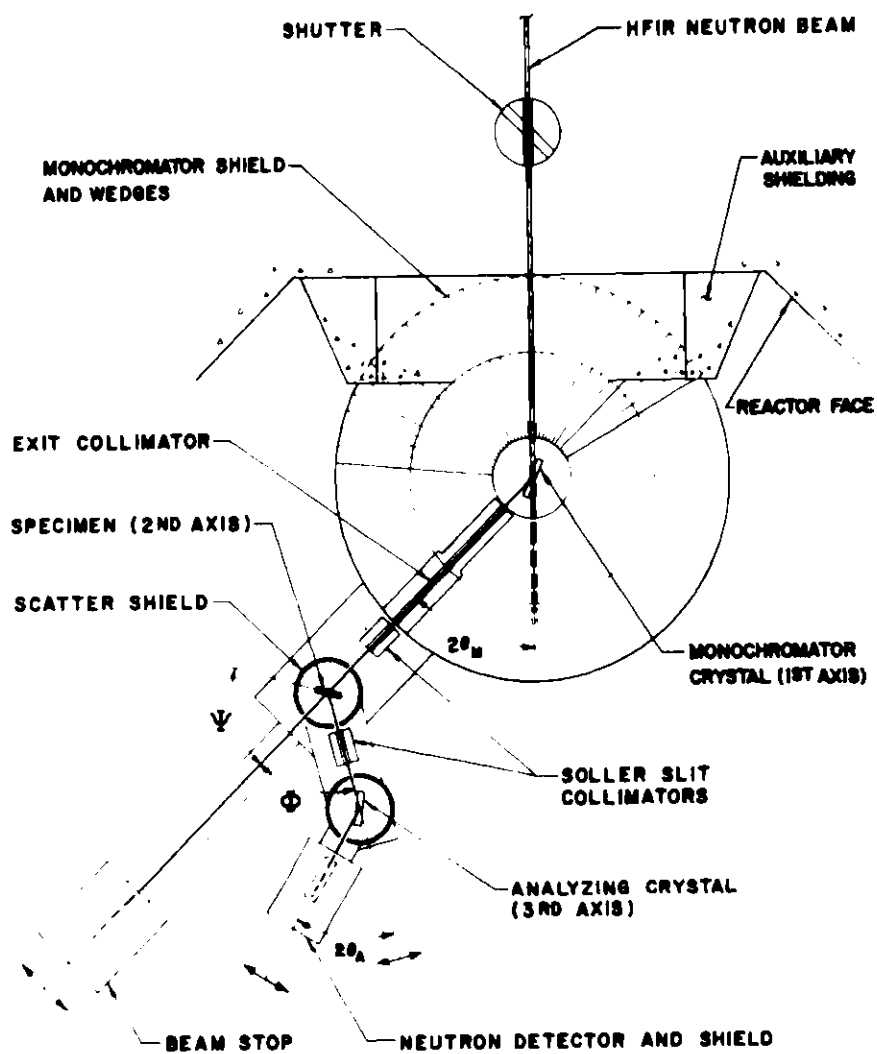


Figure 3. Schematic Diagram of the Triple-Axis Spectrometer at the High Flux Isotope Reactor (viewed from above)

Hence, the neutrons are detected from a process involving energy transfer $E_1 - E_0$ and momentum transfer $\vec{k}_1 - \vec{k}_0$.

A low efficiency monitor detector (less than 0.1 percent efficient) is placed between the monochromator and the sample to supply a real-time reference which compensates for reactor power fluctuations.

The low temperature experiments were made with a liquid helium cryostat. The sample was encased in an aluminum can in thermal contact with the liquid helium reservoir. The chamber containing the sample was filled with helium gas for thermal exchange with the helium bath. In the required experiments, careful temperature control was not necessary. All low temperature experiments were conducted at liquid helium temperature, 4.2° K. The temperature was monitored with copper-constantan thermocouples attached to the sample mount.

Alignment of the Sample

Accurate angular alignment of the sample and apparatus is of essential importance in inelastic scattering experiments. Prior to sample alignment, the angles of the diffractometer must be calibrated to an absolute scale reading. The alignment of the monochromator was achieved by removing the analyzer crystal and orienting the detector to view the sample position. By the use of a powder sample with a well known lattice constant (e.g., aluminum), the wavelength may be determined with precision. This value of λ is used to determine absolute angle settings of the monochromator.

The sample alignment is determined from several Bragg reflections. By the use of arc adjustments inside the cryostat the reflected intensity

is maximized. Accurate lattice parameters for the particular sample used were determined from no less than six reflections. The sample angle ψ and the scattering angle ϕ were determined from these Bragg reflection data. Polaroid photographs of the various beams provided a check on centering of the sample. Finally, analyzer angles were calibrated from the Bragg reflections.

The Interaction of Neutrons with Matter

Inelastic scattering of neutrons is the only technique which can be used to directly investigate the complete energy versus wavevector spectrum. The general formula for the scattering cross section σ in the Van Hove formalism for unpolarized neutrons is^{33,34}

$$\frac{d^2\sigma^{\text{coh}}}{d\Omega d\omega} = \left[\frac{m}{2\pi\hbar} \right]^2 \frac{k_1}{k_0} \frac{1}{2} \int_{-\infty}^{\infty} dt e^{i\omega t} \sum_{nn'} \sum_{ss'} P_s P_n \langle ns | s(0) | n's' \rangle \times \quad (47)$$

$$\times \langle n's' | a^\dagger(t) | ns \rangle$$

where

Ω = solid angle,

ω = energy change of scattered neutron,

m = mass of neutron,

n = crystal initial state,

n' = crystal final state,

s = incident neutron spin,

s' = final neutron spin,

\vec{k}_0 = initial neutron wavevector (momentum),

\vec{k}_1 = final neutron wavevector (momentum),
 P_n = probability that the crystal was in the initial state n ,
 P_s = probability that the initial neutron spin state was s ,
 $a(t)$ = scattering potential.

Apart from the nuclear spin interaction, the scattering potential is given by

$$a(t) = \alpha(t) + \vec{\sigma} \cdot \vec{\beta}(t) \quad (48)$$

where

$$\alpha(t) = \sum_i b_i e^{i\vec{Q} \cdot \vec{r}_i(t)}, \text{ the nuclear interaction,}$$

$$\vec{\beta}(t) = \sum_m e^{i\vec{Q} \cdot \vec{r}_m(t)} p_m \vec{S}_m^{\perp}(t), \text{ the magnetic interaction,}$$

$$\sum_i = \text{sum over all nuclei,}$$

$$\sum_m = \text{sum over magnetic ions.}$$

$$\vec{Q} = \vec{k}_1 - \vec{k}_0, \text{ the scattering vector,}$$

$$p_m = - \left[\frac{\gamma e^2}{2mc^2} \right] gf(Q), \text{ the magnetic scattering strength,}$$

$f(Q)$ = the magnetic atomic form factor,

g = the gyromagnetic ratio,

γ = neutron moment in nuclear magnetons,

$$\vec{S}^{\perp} = \vec{S} - \vec{Q}(\vec{S} \cdot \vec{Q}),$$

$\vec{\sigma}$ = Pauli spin matrices,

\vec{S} = the atomic spin of the magnetic ion.

The matrix elements in Equation (47) may be expanded into the following form (see Equation (48)):

$$\begin{aligned}
\sum_{nn'} P_n \sum_{ss'} P_s \langle ns | a(0) | n's \rangle \langle s'n' | a^\dagger(t) | sn \rangle = \\
= \sum_{ns} P_n P_s \langle sn | \{ a(0) \alpha^\dagger(t) + \vec{\sigma} \cdot \vec{\beta}(0) \vec{\sigma} \cdot \vec{\beta}^\dagger(t) \\
+ \alpha(0) \vec{\sigma} \cdot \vec{\beta}^\dagger(t) + \vec{\sigma} \cdot \vec{\beta}(0) \alpha^\dagger(t) \} | sn \rangle .
\end{aligned} \tag{49}$$

Terms in the cross section which are linear in the polarization $\vec{\sigma}$ must vanish as a consequence of the inversion symmetry of the two sublattices. Therefore, Equation (49) becomes

$$\sum_{ns} P_s P_n \{ \langle sn | \alpha(0) \alpha^\dagger(t) | sn \rangle + \langle sn | \vec{\sigma} \cdot \vec{\beta}(0) \vec{\sigma} \cdot \vec{\beta}^\dagger(t) | sn \rangle . \tag{50}$$

The cross section can therefore be separated into a pure nuclear and a pure magnetic part. Since the theory of inelastic scattering of neutrons for these two cases has been discussed thoroughly in the literature, e.g. references 33 or 34, only the results will be presented here.

The expression for the inelastic scattering of unpolarized neutrons for one magnon processes is

$$\begin{aligned}
\frac{d^2 \sigma_{\text{coh}}}{d\Omega d\omega} = \left[\frac{e^2}{mc} \right]^2 \frac{(2\pi)^3}{V} S \sum_{q\tau} (1 + \cos^2 \alpha) \frac{k_1}{k_0} |f(Q)|^2 \times \\
\times \left(n + \frac{1}{2} \pm \frac{1}{2} \right) \delta(\hbar\omega \mp \hbar f) \delta(\vec{Q} + \vec{q} - \vec{\tau}) e^{-2W}
\end{aligned} \tag{51}$$

where

α = the angle between the magnetic moment and the scattering vector \vec{Q} ,

S = spin on the magnetic ion,

$n = (e^{-\hbar f/kT} - 1)^{-1}$ is the thermal population number of the excitation,

f = the frequency associated with the magnon,

W = the Debye-Waller factor for the magnetic ion,

$\hbar\vec{q}$ = the momentum transfer associated with the excitation,

V = the volume of the unit cell.

This expression is valid for a simple antiferromagnet with two interpenetrating sublattices. The magnetic excitations will be strongest at small scattering angles (small Q) and a factor of two may be gained by orienting the magnetization direction along the scattering vector ($\cos\alpha = 1$).

The differential coherent scattering cross section for a one-phonon process in a crystal is³⁴

$$\frac{d^2\sigma_{\text{coh}}}{d\Omega d\omega} = \frac{(2\pi)^3}{V} \sum_{qs} \frac{k_1}{k_0} \frac{\hbar(n_s + \frac{1}{2} \pm \frac{1}{2})}{2f_s} |F_s(Q)|^2 \times \quad (52)$$

$$\times \delta(\vec{Q} \pm \vec{q} - \vec{\tau}) \delta(\hbar\omega \pm \hbar f_s)$$

where

$\hbar f_s = \hbar f_s(\vec{q})$ = the energy associated with the s^{th} phonon mode at \vec{q} ,

\vec{q} = the phonon wavevector or momentum transfer,

s = the phonon mode identifier,

$\vec{\tau}$ = a reciprocal lattice vector,

$F_s(Q)$ = the inelastic structure factor,

n_s = the thermal population number of phonon s .

The \pm signs express phonon creation (upper sign) and phonon annihilation (lower sign).

The experiment is designed to investigate the \vec{q} dependence of the phonon frequency $f_s(\vec{q})$ corresponding to the delta functions of Equation (52). The inelastic structure factor is given by,

$$F_s(Q) = \sum_j b_j \vec{Q} \cdot \vec{V}_{sj}(q) e^{i\vec{r}_j \cdot \vec{r}_j} (M_j)^{-1/2} e^{-W_j} \quad (53)$$

where

b_j = scattering strength of j^{th} nucleus,

\vec{V}_{sj} = displacement vector (mass weighted) for atom j in mode s at wavevector \vec{q} ,

M_j = mass of the j^{th} atom,

W_j = Debye-Waller factor for atom j .

This structure factor determines the optimum locations in reciprocal space for experimental observation of the s^{th} phonon mode. For example, to observe the transverse acoustic mode propagating in the Λ (trigonal) direction, the zone would be chosen as follows: the maximum value for Q for $\lambda \sim 1.2 \text{ \AA}$ will occur for reciprocal lattice points just inside the circle labeled $\Phi = 120^\circ$ in Figure 4, because this is the largest scattering angle that the diffractometer will reach. In a transverse Λ -mode the atom motions are perpendicular to the Λ -direction; thus, it is desirable to have \vec{Q} perpendicular to Λ to achieve maximum $\vec{Q} \cdot \vec{V}$. This precludes the scans labeled e and f in Figure 4 as possible experimental arrangements. In an acoustic mode the displacements of the atoms are generally in phase.

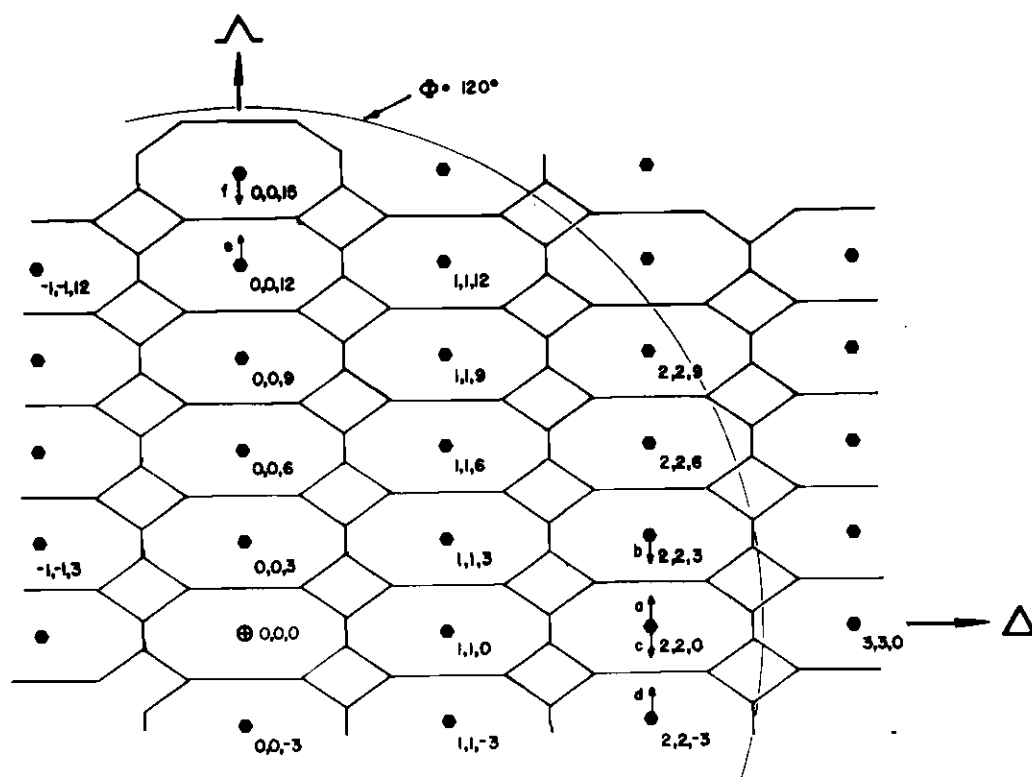


Figure 4. Scattering Plane in FeCO_3 Containing the Threefold and the Twofold Axes

It is thus desirable to scatter near an "even" reciprocal lattice point ($h+k+l=\text{even}$) to avoid cancellation arising from the exponential in the inelastic structure factor. Consequently, scans a or c are preferred to b or d (Figure 4) for a transverse acoustic phonon. For a transverse optic phonon, an "odd" reciprocal lattice point is preferred, since the atom displacements are out of phase, e.g. scan b or d. For a longitudinal Λ -phonon scan e and f would be optimum for acoustic and optic modes, respectively. The choice between the "equivalent" transverse scans a and c is made from resolution function focusing considerations to be discussed below.

The scattering cross section is inversely proportional to the energy associated with the phonon mode. This is of great importance in determining whether there will be sufficient intensity to produce an observable neutron group. Nothing can be done with respect to experimental design to overcome this difficulty. Fortunately, in the study of iron carbonate intensity limitations have never been a serious problem.

Resolution Function Focusing

Cooper and Nathans³⁵ have shown that an instrumental resolution function may be typically described by an ellipsoidal surface of constant probability in $\vec{q} - \omega$ space. This resolution ellipsoid is a function of the divergence of the beam resulting from each collimator in the system, and the mosaic spread of the monochromator, sample, and analyzer. For triple-axis spectrometers in the standard configuration the resolution ellipsoid has the following properties³⁶:

1. Two axes of the ellipsoid are typically an order of magnitude larger than the other two.

2. One of the large axes is often nearly in the $y - \omega$ plane, (x defined along the scattering vector, z out of the scattering plane), and is between approximately 5° and 20° from the ω -axis (for energy transfer small compared to E_0).

3. The other large axis is in the z direction.

4. The larger of the two short axes is close to the x axis.

The orientation of this "cigar shaped" resolution function gives rise to neutron group focusing. Focusing for longitudinal phonons is less than for transverse phonons. This characteristic is a result of property 4 and is termed "Q"-focusing (Figure 5). The experimenter has only limited control over this form of focusing by performing scans that are not 'pure' longitudinal. "Gradient" focusing occurs when the resolution ellipsoid has its long axis (property 2) in the dispersion surface. For this case, in a relatively short scan the resolution function will pass through the dispersion surface quickly, giving rise to a sharply peaked neutron group. The experimenter can control gradient focusing effects (Figure 5) by choosing the scan in the correct relationship to the reciprocal lattice point. For example, at the HFIR, a scan along the line a in Figure 4 led to more sharply peaked neutron groups than along the line c. Whenever possible, focusing effects were considered in experimental design.

Data Collection Method

All experiments were conducted in the Constant-Q or Constant-E method of scanning, illustrated in Figure 6. In the former mode, the

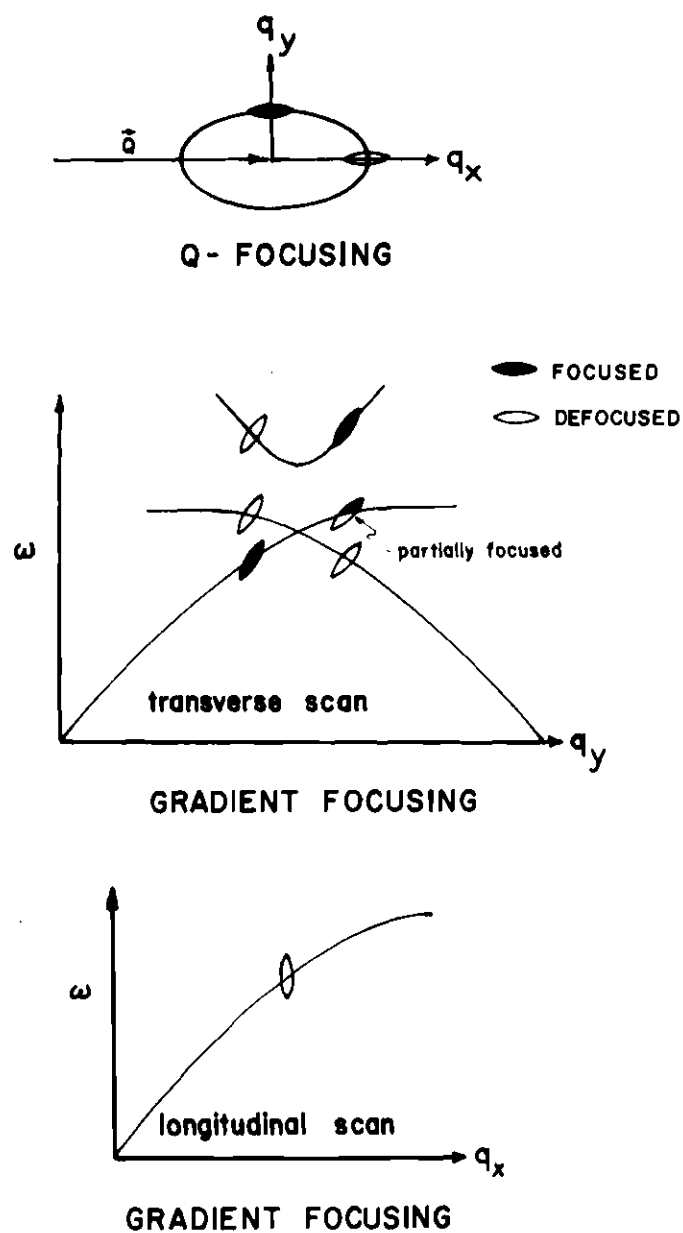
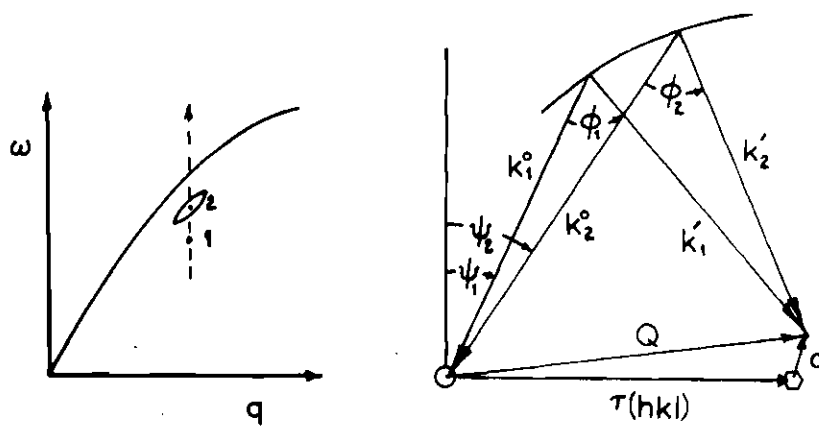
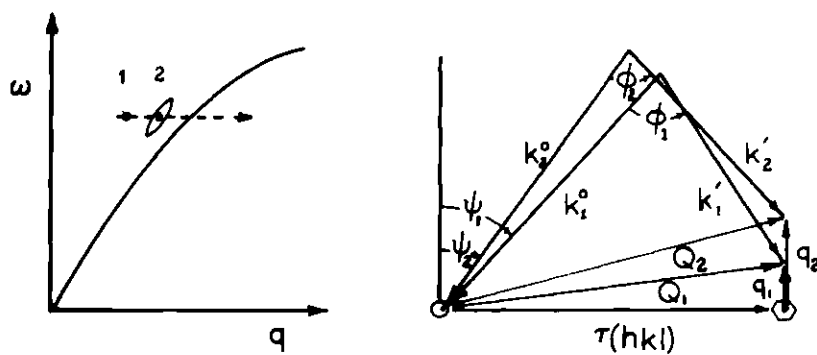


Figure 5. Resolution Function Focusing Effects in Triple-Axis Neutron Diffractometry



"CONSTANT-Q" SCAN



"CONSTANT-E" SCAN

Figure 6. Constant-Q and Constant-E Methods of Scan

scattering vector, \vec{Q} , and therefore the propagation vector, \vec{q} , is held constant while the energy transfer is varied:

$$\hbar\omega = \frac{\hbar^2}{2m_0} (k_1^2 - k_0^2) . \quad (54)$$

A constant-Q scan is equivalent to scanning along a vertical line in $\vec{q} - \omega$ space as shown in Figure 6, and a constant-E scan is equivalent to scanning along a horizontal line. These scans are accomplished by changing the angles of two of the axes of a triple-axis spectrometer. The angles are calculated with the relationships

$$Q_x = k_0 \cos\psi - k_1 \cos(\psi + \phi) \quad (55)$$

$$Q_y = k_0 \sin\psi - k_1 \sin(\psi + \phi)$$

along with Equation (54). For relatively flat (ω weakly dependent on \vec{q}) dispersion surfaces, the constant-Q mode of scanning yields the best resolution, whereas for steep surfaces the constant-E method gives the more sharply focused neutron groups.

Contamination

In inelastic scattering experiments using a triple-axis spectrometer, it is possible to observe neutron groups that result from a spurious scattering process. For example, it may happen that the angles ϕ and ψ , in an inelastic scan, may be appropriate for a Bragg reflection in the sample. If this elastically scattered beam is incident upon the analyzer, even though it is set for non-elastic reflection, incoherent processes

will scatter neutrons into the detector. In order to detect this type of spurious process, a monitor was placed in the pre-analyzer position in the experiments conducted at the HFIR. This monitor (less than .1 percent efficient) supplied a reference on the total flux reflected into the analyzer and thus provided an indication of elastic reflection contaminants.

Higher order Bragg diffraction in the analyzer of incoherently scattered neutrons from the sample may lead to neutron group contamination. If the analyzer is set for Bragg diffraction of wavevector \vec{k}_1 from reciprocal lattice vector $\vec{\tau}$, higher order reciprocal lattice points can reflect higher energy neutrons: $2\vec{\tau}$ reflects $2\vec{k}_1$, etc. It is possible that the elastic incoherently scattered neutrons $\vec{k}_0 = 2\vec{k}_1, 3\vec{k}_1$, etc. lead to spurious groups. This situation can be more easily detected than the former since the values of \vec{k}_0 and \vec{k}_1 are constantly referenced. The solution is to change the analyzer energy E_1 or the monochromator energy E_0 such that $\vec{k}_0 \neq 2\vec{k}_1$ within the scan.

Another process which may be troublesome for strong scatterers like FeCO_3 is "extinction robbing" of incident flux as the beam passes through the sample. In this case, the sample is coincidentally set for elastic diffraction from a reciprocal lattice point with a large elastic structure factor. Neutrons are scattered out of the crystal, and thus the effective flux available for inelastic scattering is reduced. This may cause an apparent shift in the neutron group energy or make the group appear to be a double peak.

General contamination of the beam incident on the sample is a

further source of spurious processes. The monochromator may scatter $2\vec{k}_0$, $3\vec{k}_0$, etc. neutrons from high order Bragg planes, incoherently scatter many wavelengths, and scatter from strong phonon modes inherent to the monochromator. All of these lead to beam contamination which the sample and analyzer may scatter into the detector via the mechanisms described above.

All of the above spurious processes have been considered in analyzing experimental results. Five percent of the neutron groups contained spurious data points. These points were readily recognized and discarded.

The Samples

There was difficulty in obtaining single crystal specimens of iron carbonate. To our knowledge FeCO_3 cannot be made synthetically in a form other than a powder with particle size less than 1000 \AA .²⁵ Consequently, naturally occurring crystals from deposits in Quebec, Greenland, and Connecticut were obtained and examined with neutron diffraction, x-ray diffraction, and neutron activation techniques.

Two crystals of approximately 3 cm^3 (sample A) and 2 cm^3 (sample B) from the Quebec deposit were used in the present study. There was a significant Mn^{2+} impurity found in all samples. Susceptibility and magnetometer measurements³⁷ have shown that as little as five percent cation substitution of Fe^{2+} in MnCO_3 shows classic uniaxial antiferromagnetism with the spins aligned along the trigonal axis. Since pure MnCO_3 is weakly ferromagnetic with spins lying in the basal plane, it is apparent that the Fe^{2+} ions dominate the magnetic system. Consequently, Mn^{2+} impurities of five percent cation substitution are not expected to

influence the magnetic system of FeCO_3 in an important way. It is interesting to note that reflections, forbidden for pure FeCO_3 , were observed in the samples used, which is possibly a result of local Fe-Mn ordering. Neutron activation analysis indicates that there is less than four cation percent substitution of Mn^{2+} for Fe^{2+} . The structure was verified with x-ray and neutron diffraction techniques.

Mosaic spreads varied slightly with direction throughout all samples tested. The mosaic spread was less than 0.6° and 0.4° (full width half maximum) for samples A and B, respectively.

CHAPTER IV

RESULTS AND DISCUSSION

Presentation of the Data

Phonon and magnon spectra were measured for momentum transfer along the threefold axis (Λ -direction) and the twofold axis (Δ -direction). The Brillouin zone and the scattering plane in which most of the data were taken are illustrated in Figures 7 and 4 respectively. All data on sample A were collected at the ORR with fixed incident neutron energy. Data on sample B were collected at the HFIR with fixed scattered energy. The data presented in Table 2, Appendix A, are selected from approximately 170 neutron groups which were subjected to contamination and scattering tests. The energies and wavevectors deduced from each neutron group were obtained from nonlinear least squares analysis which employed a Gaussian curve representation of the neutron groups with a linear background function (see Appendix B). In most cases a single Gaussian curve and a constant background were sufficient for fitting to the neutron scattering data. The width of the neutron group was compared to the expected instrumental resolution function for consistency.

The phonon dispersion curve resulting from the room temperature data is shown in Figure 8 and the magnon dispersion curve at 4.2°K is shown in Figure 9. Since resolution was approximately a factor of two better for the instrument at the HFIR compared with the one at the ORR, only data taken on sample B are shown. Within experimental error, the

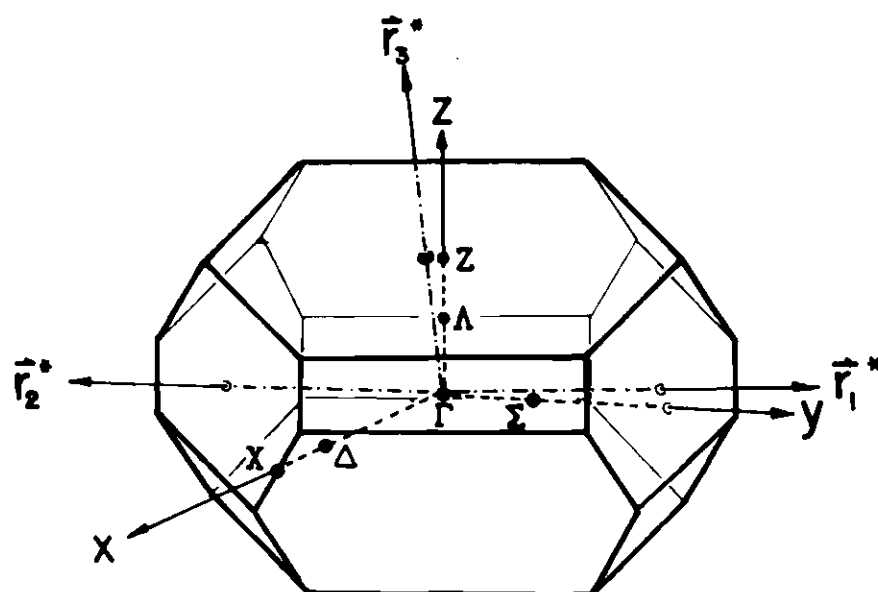


Figure 7. Brillouin Zone of FeCO_3 , Illustrating High Symmetry Lines and Points

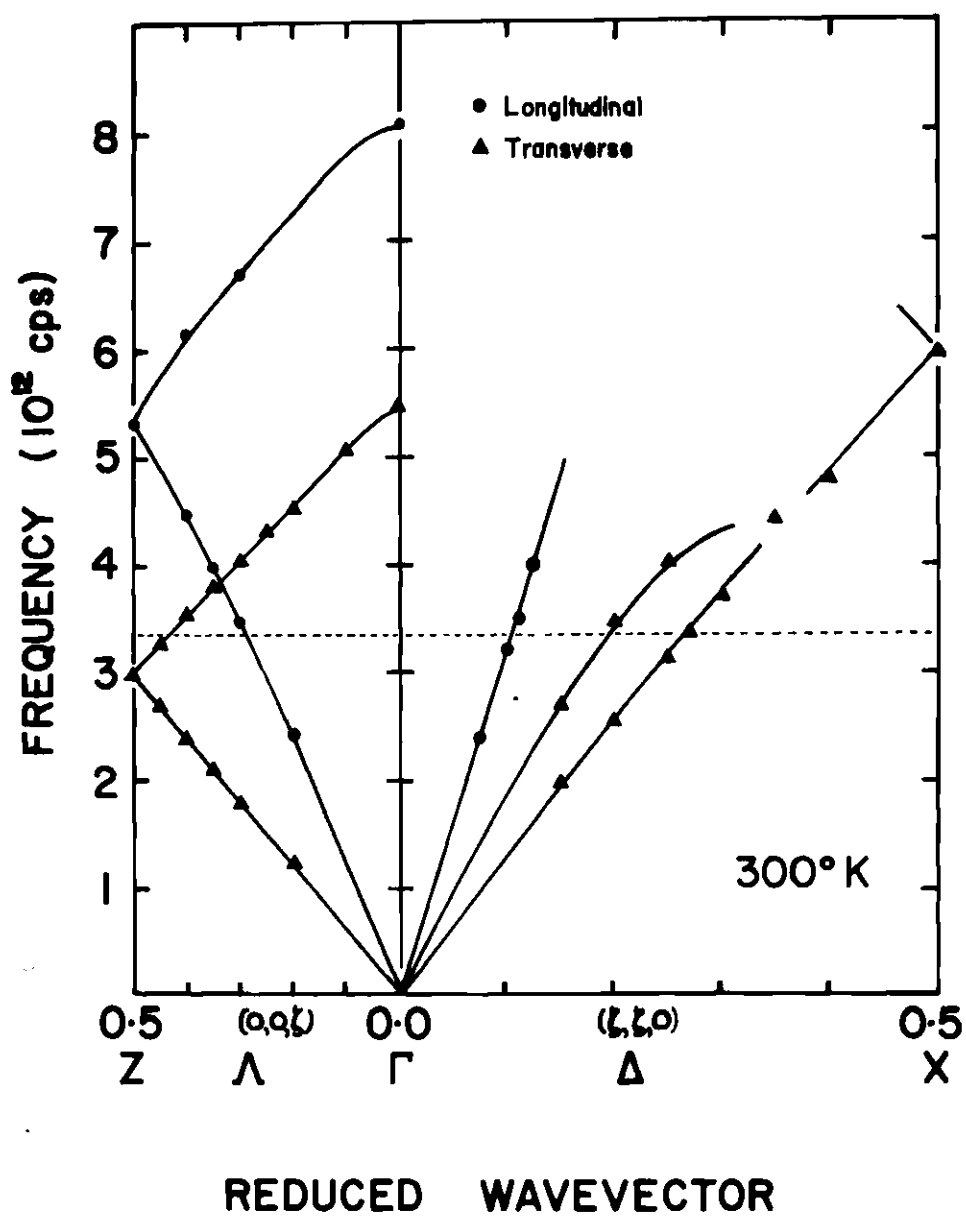


Figure 8. Phonon Spectra in the High Symmetry Directions in FeCO_3

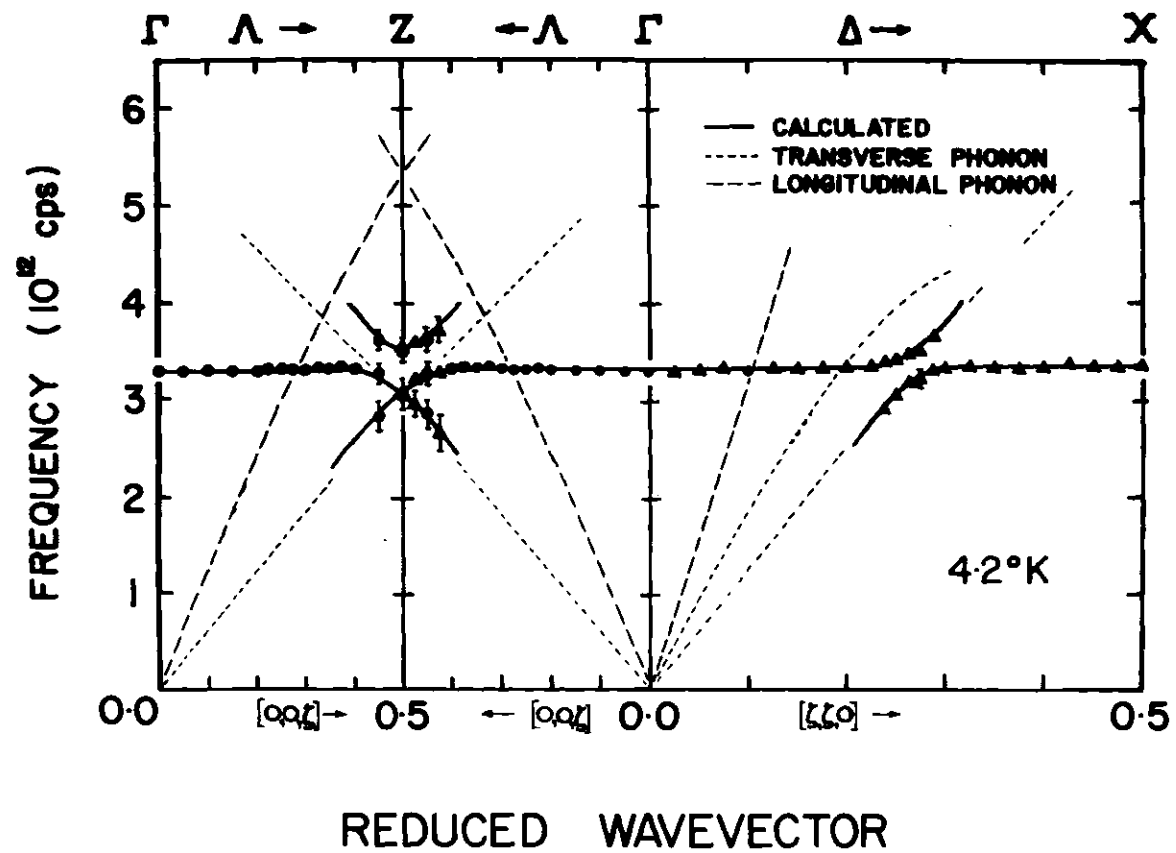


Figure 9. Magnetic Excitations Observed in FeCO_3 at 4.2°K

data for sample A agreed with the illustrated curves. In these figures the circular points represent measurements made on longitudinal modes, while triangular points indicate measurements made on transverse modes. The errors are smaller than the size of the points unless error bars are explicitly added to the data points.

The Ising Character of FeCO_3

Except in the region of phonon coupling the magnon excitation energy shows no dependence on wavevector within experimental uncertainty. In fact, as will be discussed later, the solid curve in Figure 9 representing a theoretical fit is the result of a one parameter theory in which the unrenormalized magnon dispersion curve was assumed perfectly flat. Therefore, an Ising model description of iron carbonate is experimentally verified.

For temperatures near 4.2°K , only the ground state of the magnetic ion is populated with $\langle L^z \rangle = \pm 1$, $S^z = \pm 2$.^{*} If we consider a particular ion, with say $\langle L^z \rangle = +1$, $S^z = +2$, then all of the neighbors will be in the state $\langle L^z \rangle = -1$, $S^z = -2$. For antiferromagnetic exchange with z nearest neighbors, the decrease in energy resulting from ordering will be

$$E_{\text{ex}}^g = -2JzS_i^zS_j^z = 18Jz \quad (56)$$

^{*}Henceforth we will use the value for cubic symmetry $\langle L^z \rangle = 1$ since the value of the mixing parameter θ (see Equation (8)) has not been experimentally determined for FeCO_3 . This value is expected to be within 10 percent of the correct value.

where we have used $S_{\text{tot}}^z = \langle L^z \rangle + S^z$ and Equation (11). The neutron can only cause a transition from the ground state to the first excited spin-orbit split state corresponding to $\langle L^z \rangle = 1$, $S^z = 1$ (see Figure 2). The exchange energy for six neighbors in the ground state ($\langle L^z \rangle = -1$, $S^z = -2$) with this ion will be

$$E_{\text{ex}}^1 = 12Jz . \quad (57)$$

Hence the actual energy observed will be the spin-orbit energy (related to the anisotropy energy) plus $6Jz$.

Molecular field theory predicts that the exchange constant J is related to the critical temperature via³⁸

$$kT_N = \frac{2}{3} S(S+1)z|J| . \quad (58)$$

Therefore, with $T_N = 38^\circ\text{K}$,

$$|J| = .75^\circ\text{K} \quad (59)$$

$$= .021 \times 10^{12} \text{ cps} .$$

The energy for the excitation observed is

$$E = 3.34 \pm .02 \times 10^{12} \text{ cps} \quad (60)$$

$$= 161^\circ\text{K} .$$

From Equation (59) the spin-orbit splitting parameter will be

$$|\lambda| = 123^\circ\text{K} = 89 \text{ cm}^{-1} . \quad (61)$$

An independent measurement of this quantity is unavailable for FeCO_3 . The value compares favorably, however, with typical values of spin-orbit energies of Fe^{2+} in a variety of compounds determined by Mahoney, et al.³⁹ shown in Table 1.

From Equations (61) and (34) we may write

$$E_{\text{observed}}^2 = (E_{\text{ex}} + E_{\text{s-o}})^2 - cE_{\text{ex}}^2 \gamma_k^2$$

where $E_{\text{s-o}}$ ($= 2.6 \times 10^{12}$ cps) represents the anisotropy energy, $c = 0$ for an Ising system, and $c = 1$ for a Heisenberg system. A least squares fit of this expression to the data establishes an upper limit of $c < 0.1$. These experimental results show that iron carbonate is well represented by a three-dimensional Ising system.

The Spin-Lattice Interaction

When there is an interaction between two excitations, quantum mechanical arguments show that those two excitations can never become degenerate in energy. That is, the dispersion curves of these excitations can not cross if there is a coupling between the spin system and a lattice vibration. The coupled excitation will be a combination of the excitations which would have been present in the absence of the interaction. A phonon under the influence of a spin-lattice interaction will be a combination of lattice vibration and spin fluctuation. This new excitation is termed a renormalized or dressed phonon and can be almost pure magnon or phonon in

Table 1. Spin-Orbit Splitting Parameters for Fe^{2+} Impurities in Compounds

Matrix	Spin-Orbit Splitting Parameters
ZnS	99 cm^{-1}
ZnTe	96 cm^{-1}
CdTe	99 cm^{-1}
ZnSe	85 cm^{-1}
CdSe	81 cm^{-1}

character in the Brillouin zone away from the point at which the mode would have been degenerate in the non-interacting case.

For an Ising system in the absence of a spin-lattice interaction, the fundamental magnetic excitation is a spin fluctuation of a single ion. Since S^z is a constant of the motion, there is no dynamical coupling between neighboring spins in this excitation. The spin excitation can travel through the crystal, however, through an interaction of the spin system with the lattice. In this case the propagation of the spin fluctuation is a consequence of the spin-lattice interaction rather than the $S^x S^x$ and $S^y S^y$ correlations as in a Heisenberg system.

Strong interactions are observed between the spin system and the lattice in iron carbonate. This interaction has an associated coupling energy of 0.15×10^{12} cps to 0.20×10^{12} cps, which is an order of magnitude larger than the exchange constant $|J| \approx 0.02 \times 10^{12}$ cps as determined from molecular field theory. The spin-lattice coupling only exists between the magnetic excitation and the degenerate transverse phonon mode in the Λ -direction and between the magnetic excitation and one of the transverse phonon modes in the Δ -direction. Figure 9 shows the excitations observed in these directions at liquid helium temperature.

The scans shown in Figure 10 illustrate neutron groups resulting from longitudinal scans at the crossing in the Λ -direction. The neutron group intensity will be proportional to the amount of magnon character of the excitation since the phonon cross section is proportional to $\vec{Q} \cdot \vec{V} = 0$ (see Equation (53)). Since the scan was longitudinal there is no gradient focusing so all excitations should exhibit similar widths. It can be seen

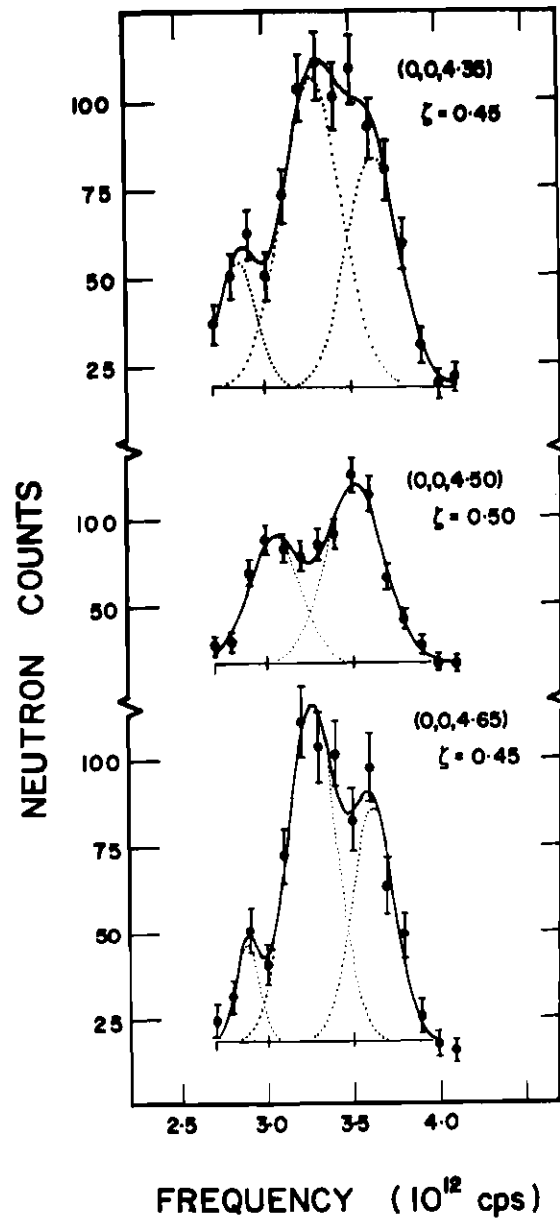


Figure 10. Typical Neutron Groups for Longitudinal Scans in the Λ -Direction Near Nominal Crossover (The numbers in parentheses indicate the coordinates of the scattering vector \vec{Q} .)

from the fitted Gaussians that the relative intensities of the observed excitations are dependent on how close the excitation is to the unrenormalized magnon energy and that the widths are indeed comparable. Transverse scans are complicated by focusing considerations and the fact that $\vec{Q} \cdot \vec{V}$ is non-zero. Nevertheless, magnon character will dominate since the scattering vector was small, resulting in a large magnetic form factor and a small inelastic phonon structure factor. Figure 11 illustrates a typical transverse scan in the Δ -direction. The neutron group widths for the higher two excitations are sharper than in the longitudinal scans discussed above, while the lower energy excitation is much broader. This is a result of gradient focusing of the upper excitations and defocusing of the lower excitation (see Figure 5).

The intensities and widths of the excitations can be more graphically observed for the coupling in the Δ -direction. All of the neutron groups in which two excitations were observed for scattering in the Δ -direction are illustrated in Figures 12 and 13. The intensity of each excitation should reflect the amount of magnon character of that renormalized mode. Thus for $\zeta = 0.238$, illustrated in Figure 12, the excitation at 3.4×10^{12} cps has the greater intensity with magnon character dominating while the lower energy excitation is almost pure phonon in character. At $\zeta = 0.250$ the excitation at 3.05×10^{12} cps has increased in intensity at the expense of the 3.45×10^{12} cps excitation. The $\zeta = 0.263$ group shown in Figure 13 occurs just before the nominal crossover point, or point of closest approach, of the two excitations. This nominal crossover occurs at $\zeta = 0.269$. Therefore the observed excitations are comparable in

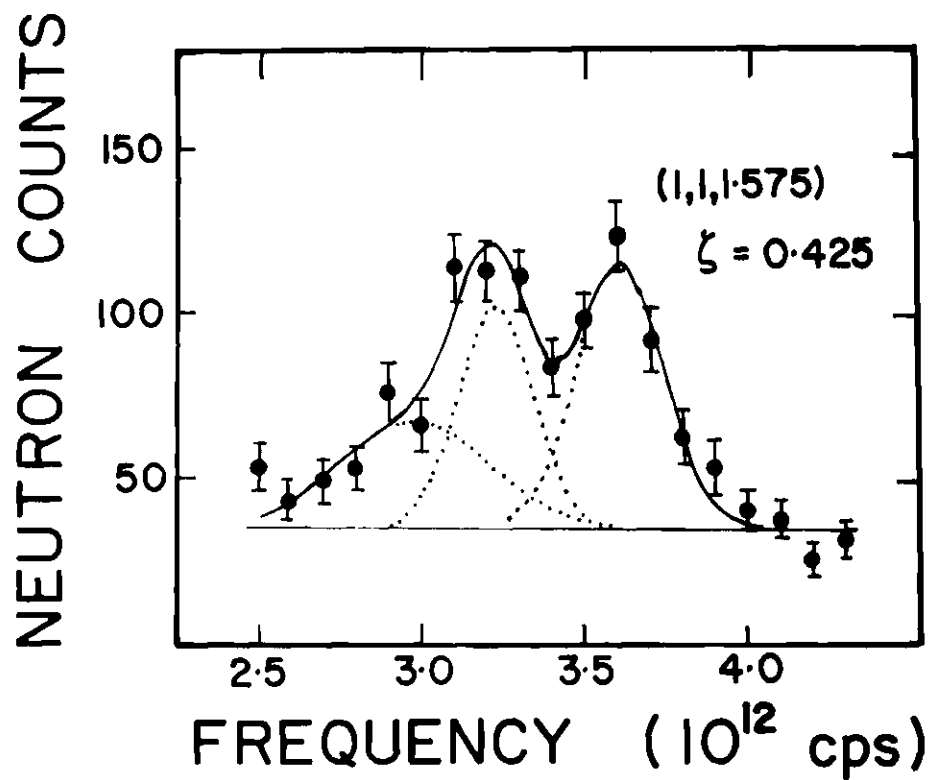


Figure 11. Typical Neutron Group for Transverse Scan in the Λ -Direction Near Nominal Crossover
(The numbers in parentheses indicate the coordinates of the scattering vector \vec{Q} .)

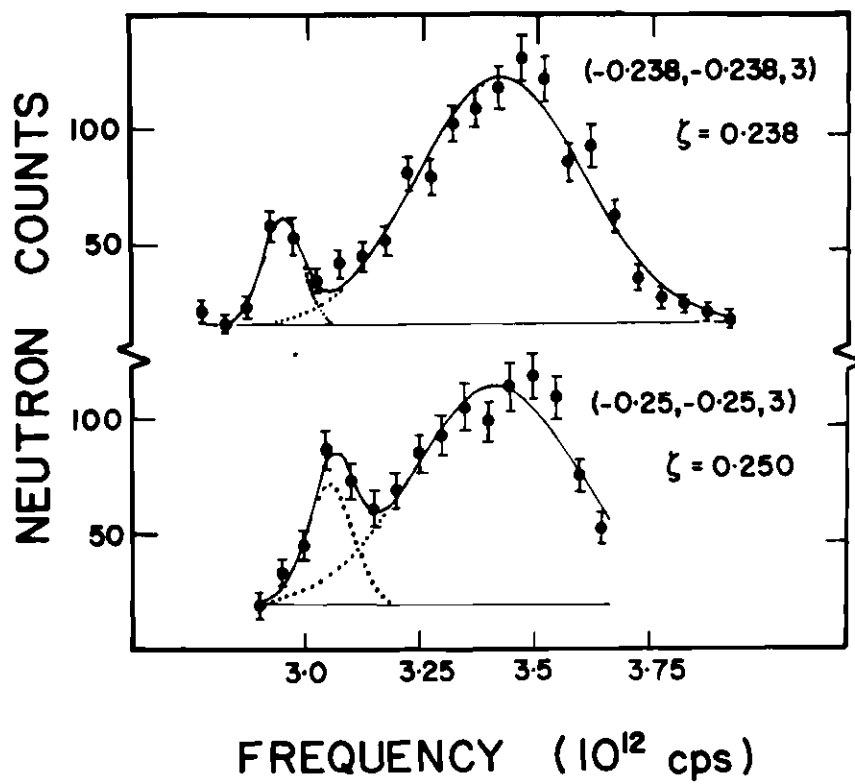


Figure 12. Neutron Groups Observed for Transverse Scans in the Δ -Direction Near Nominal Crossover (The numbers in parentheses indicate the coordinates of the scattering vector \vec{Q} .)

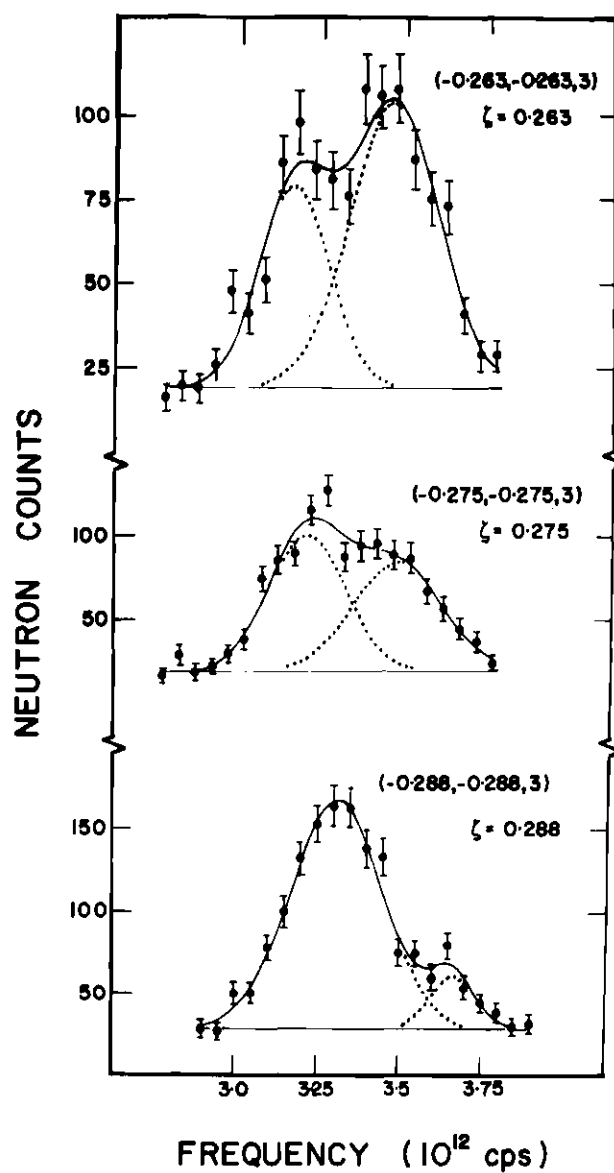


Figure 13. Neutron Groups Observed for Transverse Scans in the Δ -Direction Near Nominal Crossover
(The numbers in parentheses indicate the coordinates of the scattering vector \vec{Q} .)

intensity, with the 3.45×10^{12} cps excitation slightly stronger. The groups illustrated for $\zeta = 0.275$ and $\zeta = 0.288$ are after nominal crossover so that the magnon character of the higher energy excitation is decreasing. The observed intensity decreases for this excitation while the lower energy excitation scatters with increasing strength. The effect of gradient focusing is similarly apparent for these groups. Focusing will be best for points on the dispersion curve having the greatest slope. This is a result of the long axis of the resolution ellipsoid being tilted slightly from the energy axis. Hence, the excitation which is predominantly phonon-like should be focused better than the excitation with magnon character dominant. The neutron group widths shown in Figures 12 and 13 illustrate this dependence. The consistency in the intensity and widths of the neutron groups give added credence to the identification of the phenomenon as a spin-lattice interaction as well as verifying the validity of the fitting procedure.

The observed coupling to selective phonon modes shows that the symmetry of the irreducible representation to which the lattice vibration belongs is of critical importance. A perturbation expansion of the exchange integral in ionic displacements from equilibrium positions would not give this symmetry dependence. The coupling mechanism can be taken as a lattice vibration perturbation on the crystalline field environment of the magnetic ions.²⁰ This perturbation affects the splitting of the ionic orbital levels which is communicated to the spin system through the spin-orbit interaction.

Coupling of the spin system to the lattice through the crystal

field in FeCO_3 results in a Hamiltonian that is linear in magnon and linear in phonon variables (see Equation (38) and the preceeding section in Chapter II). The calculated renormalized energies will be given by Equations (45) and (46):

$$\omega_k^A = \omega_k^M \cos^2 \theta_k + \omega_k^P \sin^2 \theta_k - 2c_k \sin \theta_k \cos \theta_k \quad (62)$$

$$\omega_k^B = \omega_k^P \cos^2 \theta_k + \omega_k^M \sin^2 \theta_k + 2c_k \sin \theta_k \cos \theta_k$$

where

$$\tan 2\theta_k = \frac{2c_k}{\omega_k^P - \omega_k^M}.$$

Physically these two renormalized modes are no longer either pure magnons or phonons. The ratio of magnon to phonon character of the A mode is

$$\frac{\cos^2 \theta_k}{\sin^2 \theta_k} = \cotan^2 \theta_k$$

and for the B mode

$$\frac{\sin^2 \theta_k}{\cos^2 \theta_k} = \tan^2 \theta_k.$$

Thus the A mode is almost pure magnon-like for small wavevector and pure

phonon-like for large wavevector. Similarly, the B mode is phonon-like for small k and magnon-like for large k . At the nominal crossover point, $\theta_k = \pi/4$, the excitations have equal magnon and phonon character.

The integrated intensities of the fitted Gaussians for the observed neutron groups in the Δ -direction are illustrated in Figure 14. The experimental parameters for this set of scans was such that the phonon cross section was negligible compared to the magnon cross section. Therefore, the observed intensity is a measure of the magnon character of the excitation. For a pure Ising system the cross section for one magnon creation at fixed temperature is proportional to the atomic form factor and the spin direction, all other factors being constant for fixed k_1 . Hence the observed intensity should be

$$I = I_m = I_o |f(Q)|^2 (1 + \cos^2 \alpha) . \quad (63)$$

With the spin-lattice interaction this expression must be multiplied by the degree of magnon character of the renormalized excitation. Using Equation (62) the observed intensity for the A excitation should therefore be

$$I_A = I_m \cos^2 \theta_k = I_o |f(Q)|^2 (1 + \cos^2 \alpha) \cos^2 \theta_k \quad (64)$$

and the intensity for the B excitation should be

$$I_B = I_m \sin^2 \theta_k \quad (65)$$

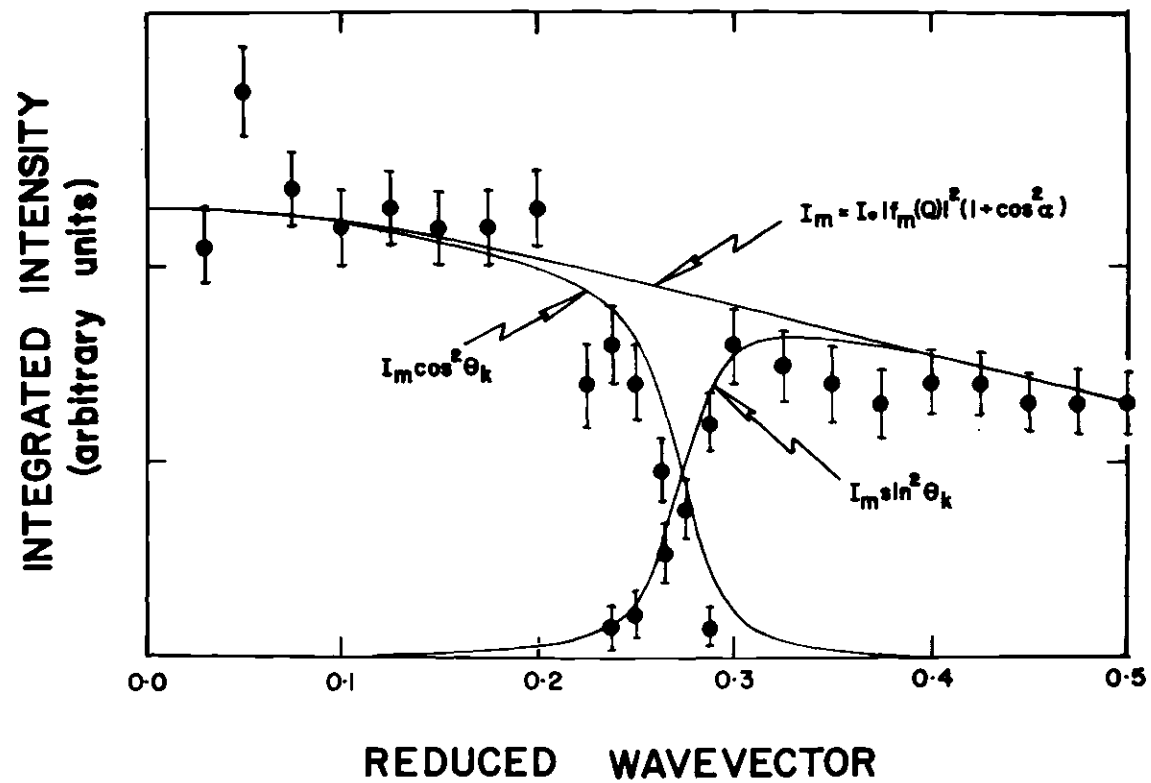


Figure 14. Integrated Intensities of Neutron Groups in the Δ -Direction Indicating the Degree of Magnon Character

The observed intensities agree quite well with the calculated curves as illustrated in Figure 14. In the calculation of I_m the form factor used was the result of a free ion Hartree-Fock calculation for Fe^{2+} with a quenched orbital moment.⁴⁰ It is evident that the Hamiltonian defined by Equation (38) is a reasonably accurate description of the spin-lattice interaction since it predicts neutron group intensities quantitatively.

The solid curves in Figure 9 are the result of fitting the calculated expressions given in Equation (62). The phonon dispersion relations observed experimentally at room temperature are illustrated by dashed lines. The degenerate transverse mode in the Λ -direction is observed to have energies which are slightly too small to be consistent with the low temperature magnon data near the crossing. This inconsistency is the result of a temperature dependence of the energies of this mode. Data taken while the cryostat was warming up from liquid nitrogen temperatures verified that a temperature renormalization is justified for this mode. Figure 15 compares the results of the room temperature measurements (circular points) with the data taken during warm up (triangular points). The temperature of the latter runs varied from 90°K to 150°K for the duration of the data run. As expected there is an inverse energy dependence on temperature. The dash-dot line in this figure is the projected dispersion relation of the transverse mode at helium temperatures used for the calculation of spin-lattice renormalized energies. Interestingly, the phonon modes in the Λ -direction did not seem to have an appreciable temperature renormalization.

The calculated curves of Figure 9 are the result of a fit of the

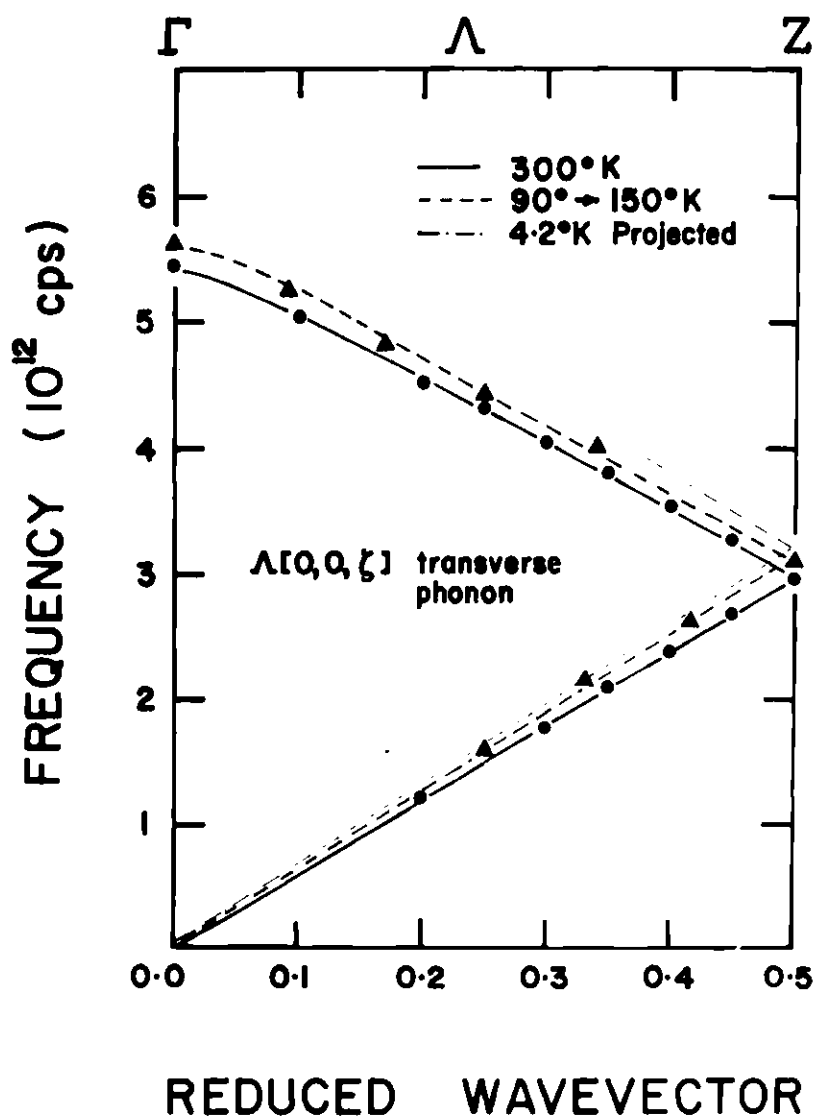


Figure 15. Transverse Phonon Dispersion Curve in the Λ -Direction as a Function of Temperature

coupling parameter c_k in Equation (62). The unrenormalized magnon dispersion relation ω_k^M was assumed to have no wavevector dependence as expected for an Ising system; it was fixed at $\omega_k^M = 3.34 \times 10^{12}$ cps. The phonon dispersion relations were linear in the region of the crossing (within experimental error). The phonon dispersion relations used were

$$\omega_k^P(\Delta) = 12.4 \times \zeta (10^{12} \text{ cps})$$

and

$$\omega_k^P(\Lambda) = 6.25 \times \zeta (10^{12} \text{ cps}) .$$

The values of the coupling parameters were determined to be

$$c_k(\Lambda) = 0.20 \pm .02 \times 10^{12} \text{ cps}$$

$$c_k(\Delta) = 0.15 \pm .02 \times 10^{12} \text{ cps}$$

by the fitting procedure. These fitted curves lie within experimental error of all measured points in both the Λ - and Δ -directions, as shown in Figure 9.

CHAPTER V

CONCLUSIONS AND RECOMMENDATIONS

Neutron inelastic scattering measurements of the magnetic dispersion relations along the two high-symmetry directions establish experimentally that the magnetic system in FeCO_3 is accurately described by the Ising model Hamiltonian. These results are fully explained within the theoretical framework established by Kanamori²⁷ and Okiji and Kanamori,²⁸ who suggested the Ising model description.

Detailed analysis of the magnetic and lattice cooperative modes establishes the existence of a strong spin-lattice interaction with a coupling strength an order of magnitude larger than the exchange integral. The coupling is observed to be dependent on the symmetry of the phonon mode; coupling only involved the transverse mode propagating along the threefold axis and one of the transverse modes propagating in the twofold direction. This symmetry dependence excludes the description of the spin-lattice interaction by a perturbation expansion of the exchange integral in ion displacements. The spin-lattice coupling mechanism is described by a lattice perturbation acting through the crystalline field which is coupled to the spin system by the spin-orbit interaction. The resulting Hamiltonian, describing the spin-lattice interaction, has coupling terms linear in the magnon operators and linear in the phonon operators. Quantitative agreement was obtained with the observed scattering data for renormalized excitations resulting from this Hamiltonian.

The fact that FeCO_3 is a physical realization of a three-dimensional Ising model suggests useful extensions of this work, especially if more nearly perfect samples could be obtained. Among the extensions to this work are spin-spin correlation measurements near the critical temperature, refined specific heat and susceptibility measurements, and investigations of the behavior of the system in an external magnetic field. The ordering phenomenon should be an extremely interesting phenomenon as a result of the strong magnetocrystalline anisotropy. For example, the persistence of sublattice magnetization may be measurable well above the ordering temperature. Two-magnon scattering^{41,42} of neutrons should be observable as a consequence of the lack of dispersion of the excitations. Lattice dynamics of the carbonates CaCO_3 , MnCO_3 , and FeCO_3 appear to be an interesting area of study. Large differences were observed between FeCO_3 and CaCO_3 for the low lying phonons and suggest that the 3d electrons may play a significant role in lattice dynamics. The phonon spectra of FeCO_3 determined in this work are compared in Figure 16 to the spectra of CaCO_3 determined by Cowley and Pant.⁴³ Optical Raman and infrared scattering studies in FeCO_3 can be expected to yield quantitative information on the crystalline field splittings postulated by Kanamori and Okiji.²⁸

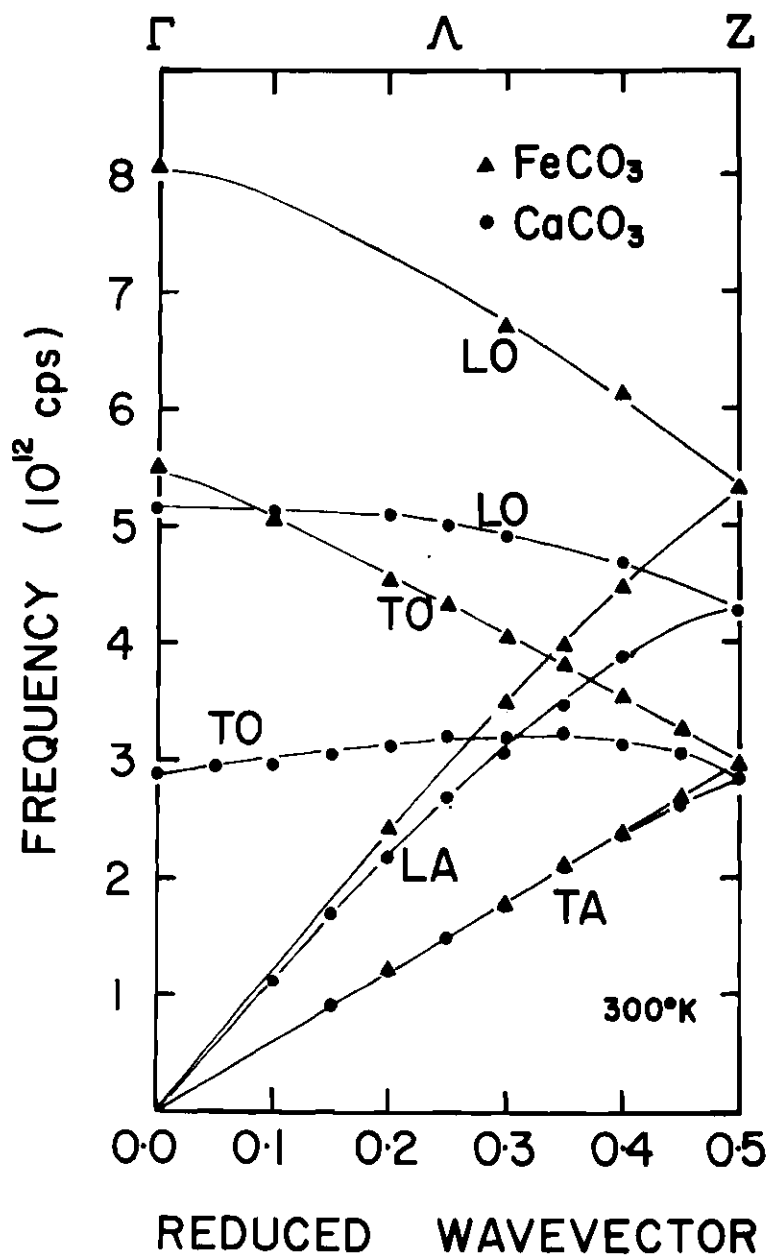


Figure 16. Phonon Dispersion Relations in FeCO_3 and CaCO_3 in the Λ -Direction

APPENDICES

APPENDIX A

PRESENTATION OF THE DATA

The data presented in Table 2 are the results of a non-linear least squares fitting program of up to three Gaussians and a background function containing up to cubic terms. The fitting technique is described in Appendix B. Each line in the table represents the results of a single, or the average of several, neutron group fits. Each group is labeled for symmetry direction, reduced wavevector, mode of scan, temperature, reciprocal lattice point from which the excitation was measured, and the sample used. Under mode of scan the letter Q denotes a constant-Q scan, E denotes a constant-E scan, L denotes a longitudinal scan (the scattering vector \vec{Q} parallel to the excitation wavevector \vec{q}), and T denotes a transverse scan ($\vec{Q} \perp \vec{q}$). All data on sample A were collected at the ORR with fixed incident energy. All data on sample B were collected at the HFIR with fixed scattered energy.

The notation relating to temperature needs to be explained. The final excitation curve analysis indicated that there is a phonon temperature renormalization in the transverse Λ mode. Unfortunately, phonon data were not taken at 4.2°K. However, one sequence of scans at the ORR was taken as the cryostat warmed from nitrogen to room temperature. This scan is labeled "90-150"°K in the data. Since the analysis contained in this work is not dependent on accuracies in the phonon data exceeding the apparent renormalization energy, these data were included to supply justification that renormalization was present.

Table 2. Excitations in FeCO_3 Determined by Neutron Inelastic Scattering

Mode Label	Reduced Wavevector (ζ units)	Energy (10^{12} cps)	Mode of Scan [†]	Lattice Point Used	Temperature ($^{\circ}\text{K}$)	Sample
Γ	(0,0,0)	$3.30 \pm .03$	Q	(0,0,3)	4.2	B
	(0,0,0)	$3.34 \pm .04$	Q	(0,0,3)	4.2	A
Λ	(0,0,0.050)	$3.30 \pm .02$	L-Q	(0,0,3)	4.2	B
	(0,0,0.100)	$3.31 \pm .02$	L-Q	(0,0,3)	4.2	B
	(0,0,0.100)	$3.34 \pm .04$	L-Q	(0,0,3)	4.2	A
	(0,0,0.150)	$3.32 \pm .02$	L-Q	(0,0,3)	4.2	B
	(0,0,0.200)	$3.31 \pm .03$	L-Q	(0,0,3)	4.2	B
	(0,0,0.200)	$3.39 \pm .05$	L-Q	(0,0,3)	4.2	A
	(0,0,0.225)	$3.34 \pm .02$	L-Q	(0,0,3)	4.2	B
	(0,0,0.250)	$3.34 \pm .02$	L-Q	(0,0,3)	4.2	B
	(0,0,0.275)	$3.33 \pm .02$	L-Q	(0,0,3)	4.2	B
	(0,0,0.300)	$3.32 \pm .02$	L-Q	(0,0,3)	4.2	B
	(0,0,0.300)	$3.37 \pm .04$	L-Q	(0,0,3)	4.2	A
	(0,0,0.325)	$3.35 \pm .02$	L-Q	(0,0,3)	4.2	B
	(0,0,0.350)	$3.35 \pm .02$	L-Q	(0,0,3)	4.2	B
	(0,0,0.375)	$3.36 \pm .02$	L-Q	(0,0,3)	4.2	B
	(0,0,0.400)	$3.34 \pm .02$	L-Q	(0,0,3)	4.2	B
	(0,0,0.400)	$3.42 \pm .06$	L-Q	(0,0,3)	4.2	A
	(0,0,0.450)	$3.63 \pm .10$	L-Q	(0,0,3)	4.2	B
		$3.28 \pm .09$				
		$2.84 \pm .15$				

[†] Q denotes constant-Q scan
 E denotes constant-E scan
 L denotes longitudinal scan
 T denotes transverse scan

Table 2. (continued)

Mode Label	Reduced Wavevector (ζ units)	Energy (10^{12} cps)	Mode of Scan [†]	Lattice Point Used	Temperature ($^{\circ}$ K)	Sample
Λ	(0,0,0.500)	3.52 \pm .07 3.05 \pm .08	L-Q	(0,0,3)	4.2	B
	(0,0,0.500)	3.55 \pm .07 3.10 \pm .15	T-Q	(1,1,0)	4.2	B
	(0,0,0.475)	3.61 \pm .06 3.23 \pm .05 2.97 \pm .14	T-Q	(1,1,3)	4.2	B
	(0,0,0.470)	3.63 \pm .13 3.19 \pm .11 2.86 \pm .17	T-Q	(1,1,3)	4.2	B
	(0,0,0.450)	3.62 \pm .10 3.26 \pm .08 2.88 \pm .13	L-Q	(0,0,6)	4.2	B
	(0,0,0.450)	3.65 \pm .09 3.31 \pm .06	T-Q	(1,1,3)	4.2	B
	(0,0,0.425)	3.73 \pm .16 3.29 \pm .12 2.66 \pm .20	T-Q	(1,1,3)	4.2	B
	(0,0,0.400)	3.73 \pm .18 3.31 \pm .17	L-Q	(0,0,6)	4.2	A
	(0,0,0.400)	3.34 \pm .02	L-Q	(0,0,6)	4.2	B
	(0,0,0.375)	3.37 \pm .03	L-Q	(0,0,6)	4.2	B
	(0,0,0.350)	3.35 \pm .02	L-Q	(0,0,6)	4.2	B
	(0,0,0.325)	3.36 \pm .02	L-Q	(0,0,6)	4.2	B
	(0,0,0.300)	3.34 \pm .02	L-Q	(0,0,6)	4.2	B
	(0,0,0.300)	3.39 \pm .06	L-Q	(0,0,6)	4.2	A
	(0,0,0.275)	3.33 \pm .02	L-Q	(0,0,6)	4.2	B
	(0,0,0.250)	3.33 \pm .02	L-Q	(0,0,6)	4.2	B
	(0,0,0.225)	3.35 \pm .02	L-Q	(0,0,6)	4.2	B
	(0,0,0.200)	3.33 \pm .02	L-Q	(0,0,6)	4.2	B
	(0,0,0.200)	3.32 \pm .03	L-Q	(0,0,6)	4.2	A
	(0,0,0.100)	3.32 \pm .03	L-Q	(0,0,6)	4.2	B

Table 2. (continued)

Mode Label	Reduced Wavevector (ζ units)	Energy (10^{12} cps)	Mode of Scan [†]	Lattice Point Used	Temperature ($^{\circ}$ K)	Sample
Γ	(0,0,0.100)	$3.26 \pm .06$	L-Q	(0,0,6)	4.2	A
	(0,0,0.050)	$3.31 \pm .02$	L-Q	(0,0,6)	4.2	B
	(0,0,0)	$3.30 \pm .03$	Q	(0,0,6)	4.2	B
	(0,0,0)	$3.29 \pm .05$	Q	(1,1,0)	4.2	B
Δ	(.025,.025,0)	$3.30 \pm .02$	T-Q	(0,0,3)	4.2	B
	(.050,.050,0)	$3.32 \pm .02$	T-Q	(0,0,3)	4.2	B
	(.075,.075,0)	$3.34 \pm .02$	T-Q	(0,0,3)	4.2	B
	(.100,.100,0)	$3.32 \pm .02$	L-Q	(1,1,0)	4.2	B
	(.125,.125,0)	$3.34 \pm .02$	T-Q	(0,0,3)	4.2	B
	(.150,.150,0)	$3.33 \pm .02$	T-Q	(0,0,3)	4.2	B
	(.175,.175,0)	$3.34 \pm .02$	T-Q	(0,0,3)	4.2	B
	(.200,.200,0)	$3.35 \pm .04$	L-Q	(1,1,0)	4.2	B
	(.200,.200,0)	$3.35 \pm .02$	T-Q	(0,0,3)	4.2	B
	(.225,.225,0)	$3.37 \pm .04$	T-Q	(0,0,3)	4.2	B
	(.238,.238,0)	$3.40 \pm .03$ $2.92 \pm .04$	T-Q	(0,0,3)	4.2	B
	(.250,.250,0)	$3.42 \pm .03$ $3.06 \pm .04$	T-Q	(0,0,3)	4.2	B
	(.263,.263,0)	$3.49 \pm .04$ $3.19 \pm .05$	T-Q	(0,0,3)	4.2	B
	(.275,.275,0)	$3.51 \pm .05$ $3.23 \pm .07$	T-Q	(0,0,3)	4.2	B
	(.288,.288,0)	$3.66 \pm .04$ $3.31 \pm .02$	T-Q	(0,0,3)	4.2	B
	(.300,.300,0)	$3.32 \pm .04$	L-Q	(1,1,0)	4.2	B
	(.300,.300,0)	$3.34 \pm .02$	T-Q	(0,0,3)	4.2	B
	(.325,.325,0)	$3.35 \pm .02$	T-Q	(0,0,3)	4.2	B
	(.350,.350,0)	$3.34 \pm .02$	T-Q	(0,0,3)	4.2	B
	(.375,.375,0)	$3.33 \pm .02$	T-Q	(0,0,3)	4.2	B
	(.400,.400,0)	$3.35 \pm .04$	L-Q	(1,1,0)	4.2	B
	(.400,.400,0)	$3.34 \pm .02$	T-Q	(0,0,3)	4.2	B

Table 2. (continued)

Mode Label	Reduced Wavevector (ζ units)	Energy (10^{12} cps)	Mode of Scan [†]	Lattice Point Used	Temperature ($^{\circ}$ K)	Sample
	(.425,.425,0)	$3.38 \pm .02$	T-Q	(0,0,3)	4.2	B
	(.450,.450,0)	$3.35 \pm .02$	T-Q	(0,0,3)	4.2	B
	(.475,.475,0)	$3.35 \pm .02$	T-Q	(0,0,3)	4.2	B
	(.500,.500,0)	$3.34 \pm .02$	L-Q	(1,1,0)	4.2	B
	(.500,.500,0)	$3.36 \pm .02$	T-Q	(0,0,3)	4.2	B
Λ : LA	(0,0,.200)	$2.43 \pm .03$	L-Q	(0,0,12)	300	B
	(0,0,.250)	$2.94 \pm .05$	L-Q	(0,0,12)	300	A
	(0,0,.300)	$3.48 \pm .02$	L-Q	(0,0,12)	300	B
	(0,0,.333)	$3.79 \pm .05$	L-Q	(0,0,12)	300	A
	(0,0,.350)	$3.97 \pm .02$	L-Q	(0,0,12)	300	B
	(0,0,.400)	$4.47 \pm .02$	L-Q	(0,0,12)	300	B
	(0,0,.417)	$4.66 \pm .06$	L-Q	(0,0,12)	300	A
Z	(0,0,.500)	$5.33 \pm .02$	L-Q	(0,0,12)	300	B
	(0,0,.500)	$5.38 \pm .08$	L-Q	(0,0,12)	300	A
Λ : LO	(0,0,.417)	$5.97 \pm .12$	L-Q	(0,0,15)	300	A
	(0,0,.400)	$6.14 \pm .04$	L-Q	(0,0,15)	300	B
	(0,0,.333)	$6.45 \pm .15$	L-Q	(0,0,15)	300	A
	(0,0,.300)	$6.70 \pm .04$	L-Q	(0,0,15)	300	B
	(0,0,.167)	$7.50 \pm .20$	L-Q	(0,0,15)	300	A
Γ	(0,0,0)	$8.08 \pm .06$	Q	(0,0,15)	300	B
Λ : TA	(0,0,.200)	$1.23 \pm .02$	T-Q	(2,2,0)	300	B
	(0,0,.250)	$1.61 \pm .04$	T-Q	(3,0,0)	90-150	A
	(0,0,.300)	$1.79 \pm .02$	T-Q	(2,2,0)	300	B
	(0,0,.333)	$2.13 \pm .04$	T-Q	(3,0,0)	90-150	A
	(0,0,.350)	$2.10 \pm .02$	T-Q	(2,2,0)	300	B
	(0,0,.400)	$2.39 \pm .02$	T-Q	(2,2,0)	300	B
	(0,0,.417)	$2.58 \pm .06$	T-Q	(3,0,0)	90-150	A
	(0,0,.450)	$2.68 \pm .02$	T-Q	(2,2,0)	300	B

Table 2. (continued)

Mode Label	Reduced Wavevector (ζ units)	Energy (10^{12} cps)	Mode of Scan [†]	Lattice Point Used	Temperature ($^{\circ}$ K)	Sample
Z	(0,0,.500)	$2.97 \pm .02$	T-Q	(2,2,0)	300	B
	(0,0,.500)	$3.05 \pm .06$	T-Q	(3,0,0)	90-150	A
Λ : TO	(0,0,.450)	$3.26 \pm .03$	T-Q	(2,2,3)	300	B
	(0,0,.417)	$3.44 \pm .06$	T-Q	(3,0,-3)	90-150	A
	(0,0,.400)	$3.54 \pm .02$	T-Q	(2,2,3)	300	B
	(0,0,.350)	$3.80 \pm .03$	T-Q	(2,2,3)	300	B
	(0,0,.333)	$3.91 \pm .06$	T-Q	(3,0,-3)	90-150	A
	(0,0,.300)	$4.04 \pm .02$	T-Q	(2,2,3)	300	B
	(0,0,.250)	$4.32 \pm .03$	T-Q	(2,2,3)	300	B
	(0,0,.250)	$4.38 \pm .05$	T-Q	(3,0,-3)	90-150	A
	(0,0,.200)	$4.52 \pm .07$	T-Q	(2,2,3)	300	B
	(0,0,.167)	$4.73 \pm .06$	T-Q	(3,0,-3)	90-150	A
	(0,0,.100)	$5.05 \pm .06$	T-Q	(2,2,3)	300	B
	(0,0,.093)	$5.28 \pm .06$	T-Q	(3,0,-3)	90-150	A
Γ	(0,0,0)	$5.50 \pm .05$	Q	(2,2,3)	300	B
	(0,0,0)	$5.60 \pm .07$	Q	(3,0,-3)	90-150	A
Δ : TA	(.15,.15,0)	$2.70 \pm .02$ $1.98 \pm .02$	T-Q	(-3,3,0)	300	B
	(.20,.20,0)	$3.46 \pm .02$ $2.57 \pm .02$	T-Q	(-3,3,0)	300	B
	(.20,.20,0)	$2.53 \pm .02$	T-Q	(0,0,12)	300	B
	(.25,.25,0)	$4.02 \pm .04$	T-Q	(-3,3,0)	300	B
	(.25,.25,0)	$3.12 \pm .02$	T-Q	(0,0,12)	300	B
	(.27,.27,0)	$3.36 \pm .02$	T-Q	(0,0,12)	300	B
	(.30,.30,0)	$3.70 \pm .02$	T-Q	(0,0,12)	300	B
	(.35,.35,0)	$4.42 \pm .03$	T-Q	(-3,3,0)	300	B
	(.40,.40,0)	$4.78 \pm .05$	T-Q	(0,0,12)	300	B
	(.50,.50,0)	$5.93 \pm .05$	T-Q	(0,0,12)	300	B

Table 2. (concluded)

Mode Label	Reduced Wavevector (ζ units)	Energy (10^{12} cps)	Mode of Scan [†]	Lattice Point Used	Temperature (°K)	Sample
Δ : LA	(.073,.073,0)	$2.50 \pm .06$	L-E	(2,2,0)	300	B
	(.075,.075,0)	$2.40 \pm .08$	L-Q	(2,2,0)	300	B
	(.100,.100,0)	$3.20 \pm .04$	L-Q	(2,2,0)	300	B
	(.112,.112,0)	$3.50 \pm .04$	L-E	(2,2,0)	300	B
	(.124,.124,0)	$4.00 \pm .04$	L-E	(2,2,0)	300	B

APPENDIX B

NONLINEAR LEAST SQUARES FITTING

The analyses of the data contained in this work are dependent on a nonlinear least squares fitting to the data of the function

$$I = p_1 + p_2x + p_3 \exp \left[- \frac{(x - p_4)^2}{p_5} \right] + p_6 \exp \left[- \frac{(x - p_7)^2}{p_8} \right] \\ + p_9 \exp \left[- \frac{(x - p_{10})^2}{p_{11}} \right] ,$$

where I is the observed intensity, x is the energy (for constant- Q) or wavevector (for constant- E scans), and p_1 to p_{11} are the fitted parameters. This appendix is intended to summarize the method of least squares as developed by Bevington⁴⁴ and Busing.⁴⁵

Following Busing,⁴⁵ consider the case where m observations are made of y , denoted y_o , each for a known value of the independent variable x . It is assumed that y may be calculated from an expression of the form

$$y_c = f(p_1, p_2, \dots, p_i, \dots, x)$$

where y_c represents the calculated value and the "best" values of the parameters p_i are to be found. The "best" set of parameters is taken to be that set which minimizes

$$S = \sum_{l=1}^m w_l (y_{o1} - y_{cl})^2$$

where w_1 is a weighting factor dependent on the standard error of the 1th observation. For a statistical counting process as in neutron scattering

$$w_1 = \frac{1}{\sigma^2} = \frac{1}{y_{o1}} .$$

Assuming that $f(p_1 \dots p_n, x)$ is linear in the p_i 's, it may be shown that a set of n approximate parameter changes Δp_i which will reduce S will be a solution of the n equations

$$\sum_{j=1}^n \Delta p_j \sum_{l=1}^m \frac{1}{y_{ol}} \frac{\partial y_{cl}}{\partial p_j} \frac{\partial y_{cl}}{\partial p_i} = \sum_{l=1}^m \frac{1}{y_{ol}} \frac{\partial y_{cl}}{\partial p_i} (y_{ol} - y_{cl})$$

$$(i = 1, \dots, n) .$$

In general $f(p_1, \dots, p_n, x)$ is nonlinear in the p_i 's and the procedure must be repeated correcting the p_i 's on each cycle. Convergence is strongly dependent on an initial guess at the p_i such that $f(p_1, \dots, p_n, x)$ is near the linear region of convergence, i.e., to yield values of y_c resulting in a value of S near a minimum.

In matrix notation we must solve

$$\underline{ax} = \underline{v}$$

where

$$a_{ij} = \sum_{l=1}^m \frac{1}{y_{ol}} \frac{\partial y_{cl}}{\partial p_i} \frac{\partial y_{cl}}{\partial p_j}$$

$$x_j = p_j$$

$$v_i = \sum_{l=1}^m \frac{1}{y_{ol}} \frac{\partial y_{cl}}{\partial p_i} (y_{ol} - y_{cl}) .$$

The solution is

$$\underline{x} = \underline{a}^{-1} \underline{v} = \underline{b} \underline{v} .$$

The statistical significance of the fit will be

$$\chi^2 = \frac{S}{m - n}$$

and is known as the "standard error of an observation of unit weight."

χ should approach a value of unity at convergence with a value larger than one indicating that the errors were underestimated (too poor a fit) and a value less than unity indicating overestimation of errors (too good a fit).

The standard error of each parameter p_i may be shown to be⁴⁴

$$\sigma_{p_i} = \chi \sqrt{b_{ii}} .$$

In the neutron data from FeCO_3 a requirement imposed on all results of this fitting technique was that $.6 < \chi < 2$ before the neutron group was even considered reliable.

APPENDIX C

A COMPUTER CONTROLLED NEUTRON DIFFRACTOMETER AT THE GTRR

A computer controlled neutron diffraction facility was designed and constructed for the H-9 beam port at the research reactor (GTRR) of the Frank H. Neely Nuclear Research Center at the Georgia Institute of Technology. This facility was used as a training instrument for triple-axis inelastic scattering work on FeCO_3 and for nuclear and magnetic structure verification, sample selection, sample orientation, and general characterization of specimens. The flux available at one megawatt power was found to be sufficient for simple phonon spectroscopy experiments. The experience gained with this instrument was very beneficial in obtaining more efficient utilization of the triple-axis facilities at Oak Ridge National Laboratory.

This appendix describes some of the important features of the GTRR facility. The design philosophy is presented first, which is believed to be an innovation in the area of experimental control; a description of the hardware interface and software programming approach then follows. Finally, an example of the type of experiments which have been performed at this installation is described (a more complete set of examples is given in reference 46).

Design Philosophy

The increasing complexity of experimental design demands progressively more sophisticated control equipment. Unfortunately, this sophistication is usually gained at the expense of flexibility. Historically, the first steps in automatic experimental control were taken using hard-wired systems that attempted to control narrowly defined experiments. Necessarily the usefulness of this system was limited since the experimentalist was required to design experiments within the narrowly defined operations of the equipment.

With the advent of the small computer, an important expansion of flexibility was realized which was economically very attractive. For the first time the control hardware could be designed to fit the experiment through flexible programming (software) techniques. This kind of programming was generally written in machine language using a compiler or an assembler program. Such programming took weeks or months to complete and implement, but this approach was an improvement over the building of a sophisticated hardware system which generally required more time. Because of the specialized nature of machine language, the software system was usually written by programmers; the experimenter preferred to devote his time to experimental design and analysis. Hence, he was often confined by the programmer's concept of the operating system. Although an attempt can be made to make the software general, practical limitations lead to a design intended for a particular class of experiments.

A flexible form of software consists of a library of subroutines, containing detailed machine language programs (called handlers) to con-

trol the hardware. The logical sequence of the calling of these handlers is determined by the experimenter. It is desirable that the programming language have a syntax related to the way in which the experimenter approaches his problem rather than the way in which the computer performs its internal operations. In this approach, the experimenter need not learn a great deal about computers. The logical programming may be coded, in high level language, to control the experiment in the required manner. The high level programming requires a relatively small expenditure of time so that the experimentalist may conveniently write his own programs. The software which can fulfill these requirements is called an interpreter.⁴⁷ An interpreter translates a high level language into functional operations so that programming need never be converted into machine language.

The use of an interpreter is particularly well suited for training purposes since the novice experimenter may examine and modify the detailed logic of the control sequence. This form of control system may be less elegant than machine language coded systems in specific applications, since it is usually less efficient as a result of its interactive nature. However, the flexibility of an interpreter compensates for this annoyance.

The Hardware System

A PDP-8 computer with 8K of 12-bit word memory, manufactured by the Digital Equipment Corporation (DEC), is the basic digital processor used for the control system.⁴⁸ A simple computer interface has been constructed to control three Slo-Syn bifilar stepping motors. The interface

uses DEC "Flip-Chip" logical function modules⁴⁹ and is shown in Figure 17. Selection of motor direction and single-step commands is under program control. The stepping rate is controlled by the software. Facilities are also provided to control a neutron spin-flipper for polarized neutron apparatus and to detect several diffractometer-angle limit conditions. A complete list of machine language input-output transfer (IOT) instructions for this interface is contained in Table 3.

A sophisticated scalar-timer computer interface, designed and constructed by the Nuclear Engineering Department of the Georgia Institute of Technology, is used. This interface was intended for general experimental purposes. Two of the four 100 MHz scalars and the program-controllable timer were used for the neutron diffraction control system. The relevant parts of this interface, modified for the neutron diffraction control, are illustrated in Figures 18 and 19. In use, the computer interrogates the scalars by stepping a 12 position selector register, each step transferring three binary coded decimal (BCD) characters into the accumulator (AC). The BCD information is transferred into the AC in the following order:

SR0 : "HOME" - parity information
 SR11: scalar 1 - high order digits
 SR12: scalar 1 - middle order digits
 SR13: scalar 1 - low order digits
 SR21: scalar 2 - high order digits
 SR22: scalar 2 - middle order digits
 SR23: scalar 2 - low order digits
 SR31: scalar 3 - high order digits
 SR32: scalar 3 - middle order digits
 SR33: scalar 3 - low order digits

(Continued)

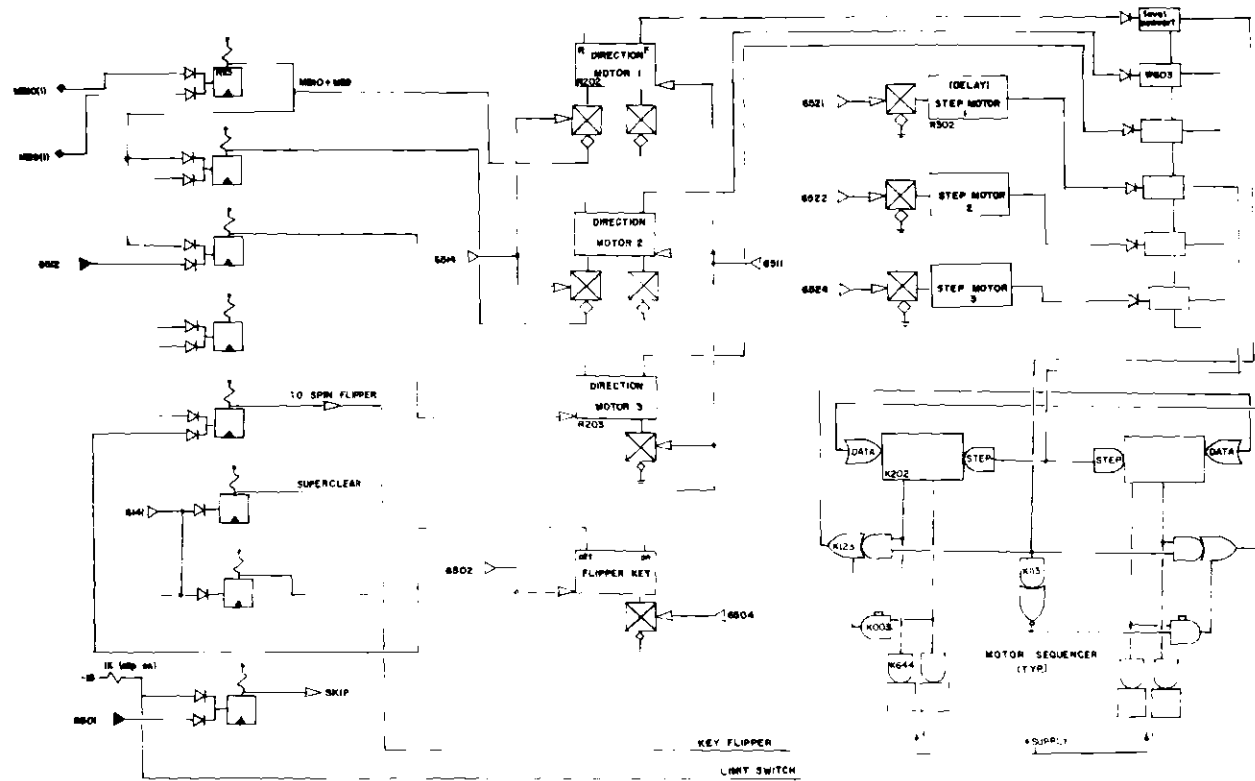


Figure 17. Logic Design for the GTRR Computer Controlled Neutron Diffraction Interface

Table 3. IOT Instructions for Neutron Diffraction Computer Control

Instruction	Description
6111	Clear time in timer control
6112	Load seconds
6114	Load milliseconds
6116	Load microseconds
6121	Skip on Timer Flag (Flag 1)
6122	Skip if Scalar disabled (Flag 2)
6125	Clear Timer Flag
6126	Scalar reset enable (clear Flag 2)
6127	Clear both flags
6132	Scalars to "HOME"
6134	Selector Register to AC and step
6141	SUPERCLEAR - clear everything
6142	Set Interrupt enable
6144	Arm Scalars
6151	Scalar Reset disable
6152	Advance Scalars
6154	Start Timer
6511	All motors forward
6512	Motor 1 reverse
6514	Motor 2 reverse
6516	Motor 3 reverse
6521	Step motor 1
6522	Step motor 2
6524	Step motor 3

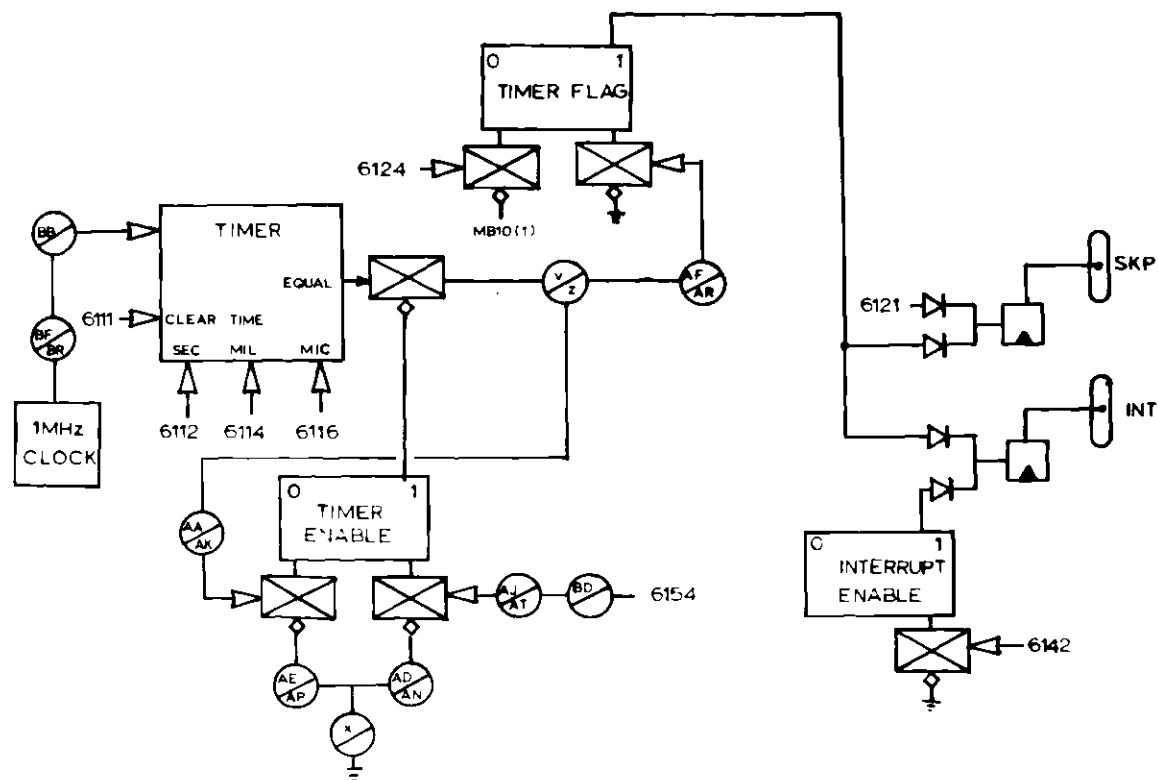


Figure 18. Logic Design and Utilization of the Scalar Timer Interface for the GTRR Computer Controlled Neutron Diffraction Interface, Part I

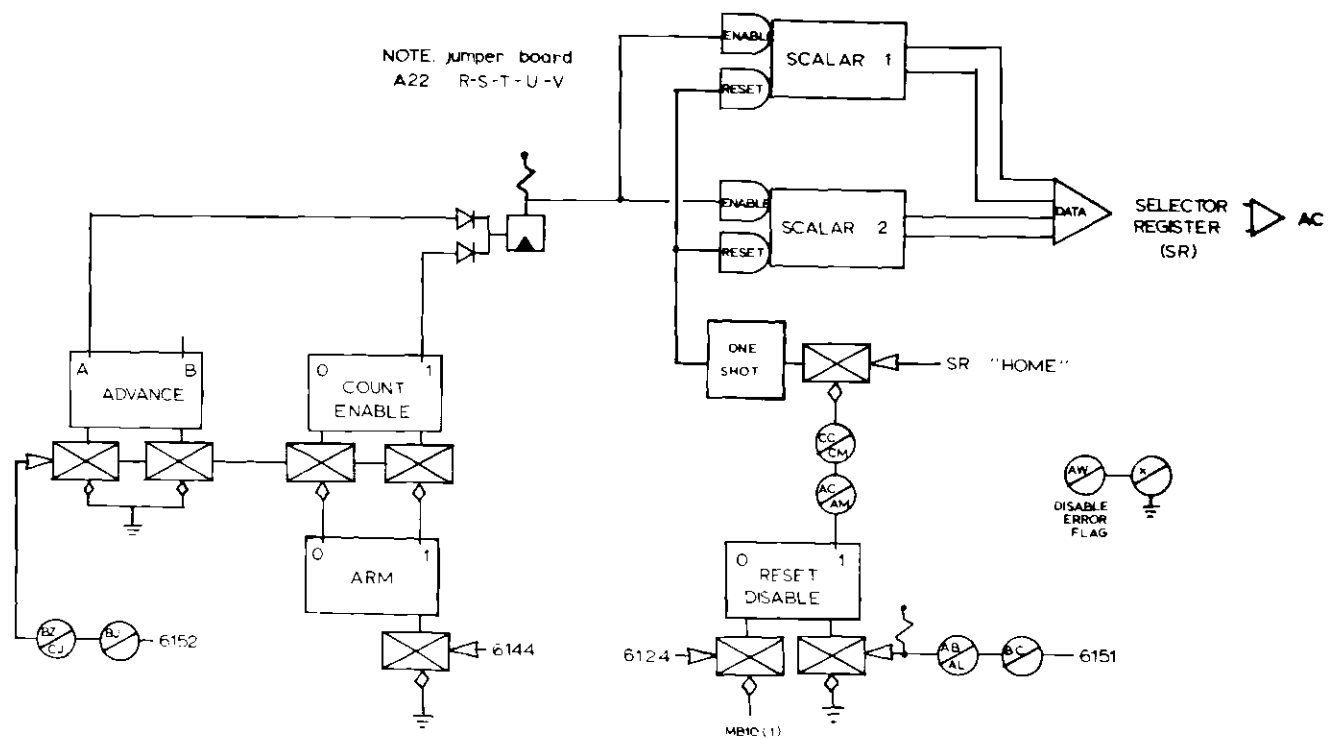


Figure 19. Logic Design and Utilization of the Scalar Timer Interface for the GTRR Computer Controlled Neutron Diffraction Interface, Part II

SR41: scalar 4 - high order digits
SR42: scalar 4 - middle order digits
SR43: scalar 4 - low order digits

The scalars are controlled by an "Arm" and "Advance" logical gate (flip-flop). The "Arm" flip-flop enables the "Advance" flip-flop which sets or resets the enable state of all scalars.

The timer may be loaded from one microsecond to 60 seconds under program control. Information is transferred from the AC to the timer in BCD. When the clock reaches the preset time, the timer flip-flop is set which may be tested and cleared under program control. This flip-flop causes an interrupt if the interrupt flip-flop is set. A special instruction, SUPERCLEAR, causes all flip-flops and other interface functions to be cleared.

The Software System

The interpreter FOCAL, developed by the Digital Equipment Corporation, was adopted as the control language for the computer-controlled diffractometer. The FOCAL language is described in references 47 and 50. The motivation for choosing this language as a basis for the control system was its syntactical orientation towards scientific problems, its short and easy-to-learn command structure, and its powerful instruction set.

A program overlay was made to the FOCAL interpreter to handle various basic functions of the hardware. These handlers were intentionally designed to operate in an unsophisticated way in order to allow maximum flexibility of the interpreter. The functions implemented are:

FADC(Arg1,Arg2,Arg3):

Arg1 = number of steps motor 1

Arg2 = number of steps motor 2

Arg3 = number of steps motor 3.

The arguments may be an arithmetic expression with absolute value less than 4095. The stepping rate is governed by a preset time interval (see FX(4,xxx.xxx)). Actual stepping is done through the interrupt service routine allowing additional computations to be executed while motor operations are in progress. The acceleration of the motors to the maximum rate is governed by a stepping rate ramping routine.

FX(4,xxx.xxx):

Sets the timer to interrupt every xxx.xxx seconds.

FCNT(Arg):

Arg=0 Reads the scalars into the FOCAL variables S' and S" leaving the run state (enable state) as before call. The scalars are disabled for approximately 100 microseconds during the read.

Arg=1 Reads the scalars as above except changes the run state of the scalars.

Arg=2 Resets and enables the scalars.

Arg=3 Returns 0 if motor is through stepping. Has the value of 3 if motor is still stepping.

FX(5):

Resets the scalars and enables them for the time period as determined by the last FX(4,xxx.xxx). At completion of this

time period the scalars are read into the FOCAL variables

S' and S'' .

We have found that the use of FOCAL is a flexible and powerful software system for running real-time experiments. Among the advantages are:

1. experimental control may be rapidly redesigned,
2. new routines may be speedily programmed,
3. inefficiencies of new program development are removed (e.g. extensive editing and assembling operations),
4. the command mode allows addressing of hardware without extensive reprogramming for initialization and set up operations,
5. each experiment can have a program explicitly designed for that experiment, and
6. the software is experimenter oriented.

Typical Operation

The language resulting from the above development gives complete control of the diffractometer to the experimenter. Use of the "command mode" of FOCAL allows addressing of the hardware for initialization and instrument alignment without the necessity for indirect programming.

A typical indirect program is illustrated in Figure 20. Several of the "groups" (a group is a set of lines having the same integer part line number) in this program are standard for most experiments. Group six is the motor moving block. The command "DO 6" will move the angles to the settings $\Phi=TH$, $\psi=OM$, and $2\theta_A=AN$. This group takes the slack out of gears by always completing an angular setting with a movement in the

C-FOCAL S 2/71

Ø1.Ø1 MAIN CONTROL OF SCANS

Ø1.1Ø F PL=.Ø5,.Ø1,.15;F PE=.5+PL*5,.Ø5,1.5+PL*5;D 5;D 6 [†K
D 7;D 8

Ø1.2Ø S PE=1.3;F PL=.Ø5,.Ø1,1.5;D 5;D 6;D 7;D 8

Ø1.5Ø QUIT

Ø5.Ø1 CALCULATE ANGLES FOR INELASTIC SCAN

Ø5.1Ø S I=57.296;S S'=PA/I [†K

S N=FSQT(PL†2+TA†2-2*PL*TA*FCOS[S'])

Ø5.2Ø S TH=PL*FSIN(S')/N;S TH=FATN(TH/FSQT[1-TH†2])

Ø5.3Ø S AN=FSQT(SL†2+N†2-2*SL*N*FCOS[TH+SA/I])

Ø5.4Ø S L=SL*FSIN(TH+SA/I)/AN;S S'=FATN(L/FSQT(1-L†2))

Ø5.5Ø S L=5.7224;S N=FSQT(L†2-1.996*PE)

Ø5.6Ø S L=(L†2+N†2-AN†2)/2*L*N;S OM=FSQT(1-L†2)*N/AN

Ø5.7Ø S OM=FATN(OM/FSQT(1-OM†2));S OM=9Ø-OM-TH-S')*I

Ø5.8Ø S TH=I*FATN(FSQT[1-L†2]/L);I (-TH)5.9;S TH=18Ø+TH

Ø5.9Ø S AN=S*I*FATN(I/FSQT[N†2*.2Ø19-1])

Ø6.Ø1 C MOTOR MOVING BLOCK

Ø6.1Ø S L=FITR(TH*55.56)-B;S S"=FITR(OM*55.56)-C [†K

S I=-FITR(AN*2ØØ)-D

Ø6.2Ø D 6.8;D 6.3;D 6.5;I (-FABS(L)-FABS(S")-FABS(I))6.1 [†K
D 6.1

Ø6.3Ø S S'=FX(4,ØØØ.ØØ1)+FADC(L,S",I);D 6.4

Ø6.4Ø I (-FCNT(3))6.4

Ø6.5Ø S B=B+L;S C=C+S";S D=D+I

Ø6.6Ø S L=2Ø*(FSGN(L)-1);S S"=2Ø*(FSGN(S")-1) [†K

S I=8Ø*(1+FSGN(I-1))

Ø6.7Ø D 6.3;S L=-L;S S"=-S";S I=-I;D 6.3

Ø6.8Ø S N=L;D 6.9;S L=N;S N=S";D 6.9;S S"=N;S N=I [†K

D 6.9;S I=N

Ø6.9Ø S N=1E3*FSGN(N)*(1+FSGN(N)-2E3))

Ø7.Ø1 C SCALAR CONTROL BLOCK WITH WAIT WHEN REACTOR DOWN

Ø7.1Ø S N=FCNT(2);S S'=Ø

Ø7.2Ø S I=S';S N=FCNT(Ø);I (S'-MC)7.3;S L=FCNT(1) [†K

T %8.ØØ,S",%6.Ø4;RETURN

Ø7.3Ø I (I+1Ø-S')7.2;I (L)7.1;T "RD";S L=-1;G 7.1

Ø8.Ø1 C "*" GRAPH

Ø8.1Ø F N=1,S"/NO;T " "

Ø8.2Ø T "*"!

Figure 20. A Typical FOCAL Program Used for Inelastic Neutron Scattering Experiments

positive direction. The command "DO 7" will reset and enable the scalars until the monitor scalar exceeds the value "MC." Group eight prints a "*" graph next to the data for preliminary data assessment, purely for convenience. Group five calculates the angular settings for any type of line scan in \vec{q} - ω space as shown in Figure 21.

In group five of Figure 20 the variables are defined by:

TH = scattering angle Φ ,

OM = sample angle ψ ,

TA = reciprocal lattice vector, $\vec{\tau}$, in \AA^{-1} (2π included in all wave-vectors),

PA = phonon angle with $\vec{\tau}$ in degrees,

PL = momentum transfer in \AA^{-1} , \vec{q} ,

PE = energy transfer in 10^{12} cps,

SL = scan length in \AA^{-1} ,

L = $2\pi/\lambda$, the incident wavevector.

To perform a constant-Q scan from .5 to 1.5×10^{12} cps the variables PA, PL, SL, SA, and TA must be defined and the command

```
FOR PE=.5,.05,1.5;DO 5;DO 6;DO 7;DO 8
```

given. To do a constant-E scan the command

```
F PL=.05,.01,.15;D 5;D 6;D 7;D 8
```

will scan from $q=.05\text{\AA}^{-1}$ to $.15\text{\AA}^{-1}$. To scan along a line in \vec{q} - ω space from Q1,W1 to Q2,W2 a valid command sequence is

```
S SL=0;F M=0,20;S PL=Q1+(Q2-Q1)*M/20 [↑K
```

```
S PE=W1+(W2-W1)*M/20;D 5;D 6;D 7;D 8.
```

Any of the above scan commands may be included in the indirect program to

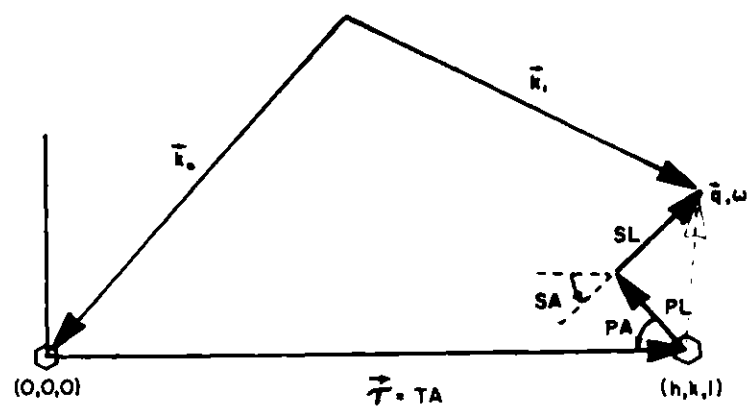


Figure 21. Schematic of the Reciprocal Space Representation of a FOCAL Controlled Inelastic Scan

perform a sequence of scans with the machine unattended. For example line 1.1 in Figure 20 collects data on a family of excitations. The illustrated program may also be used to map out a resolution function of the diffractometer by scanning in energy planes near a Bragg peak:

```
SET PA=90;SET SA=0
```

```
F PE=0,.1,1;F PL=-.1,.02,.1;F SL=-.2,.02,2;D 5;D 6;D 7.
```

Elastic data collection may be performed with the same program (Figure 20) without using group five.

In conclusion we have found that diffractometer control using a high level language, FOCAL, is extremely easy to use and highly flexible.

BIBLIOGRAPHY

1. M. E. Fisher, Reports of Progress in Physics, 30, 615 (1967).
2. J. C. Wright, H. W. Moos, J. H. Colwell, B. W. Mangum, and D. D. Thornton, Physical Review, 3, 843 (1971).
3. A. Narath and J. E. Schirber, Journal of Applied Physics, 37, 1124 (1966).
4. K. W. Mess, E. Lagendijk, D. A. Curtis, and W. J. Huiskamp, Physica, 34, 126 (1967).
5. R. F. Wielinga, H. W. J. Blöte, J. A. Roest, and W. J. Huiskamp, Physica, 34, 223 (1967).
6. S. de S. Barros and S. A. Friedberg, Physical Review, 141, 637 (1966).
7. P. D. Scott and W. P. Wolf, Journal of Applied Physics, 40, 1031 (1969).
8. S. Hüfner, L. Holmes, F. Varsanyi, and L. G. Van Uitert, Physical Review, 171, 507 (1968).
9. G. A. Prinz, Physics Letters, 20, 323 (1966).
10. H. W. J. Blöte and W. J. Huiskamp, Physics Letters, 29A, 304 (1969).
11. B. E. Keen, D. Landau, B. Schneider, and W. P. Wolf, Journal of Applied Physics, 37, 1120 (1966).
12. B. Schneider, D. P. Landau, B. E. Keen, and W. P. Wolf, Physics Letters, 23, 210 (1966).
13. A. H. Cooke, K. A. Gehring, M. J. M. Leask, D. Smith, and J. H. M. Thornley, Physical Review Letters, 14, 685 (1965).
14. G. T. Rado, Physical Review Letters, 23, 644 (1969).
15. J. C. Norvell, W. P. Wolf, L. M. Corliss, J. M. Hastings, and R. Nathans, Physical Review, 186, 557 (1969).
16. J. C. Norvell, W. P. Wolfe, L. M. Corliss, J. M. Hastings, and R. Nathans, Physical Review, 186, 567 (1969).

17. O. Nagai, Journal of the Physical Society of Japan, 18, 74 (1963).
18. H. C. Bolton and B. S. Lee, Journal of Physical Chemistry: Solid State Physics, 3, 1433 (1970).
19. R. Silberglitt, Journal of Applied Physics, 40, 1114 (1969).
20. S. Lovesay, private communication.
21. M. Foëx, Annals of Physics, 16, 174 (1921).
22. H. Bizette, Journal de Physique et le Radium, 12, 161 (1951).
23. R. A. Alikhanov, Soviet Physics--JETP, 9, 1204 (1959).
24. N. Koon, Ph.D. dissertation, Georgia Institute of Technology, 1969 (unpublished).
25. H. N. Ok, Physical Review, 185, 472 (1969).
26. I. S. Jacobs, Journal of Applied Physics, 34, 1106 (1963).
27. J. Kanamori, Progress of Theoretical Physics, 20, 890 (1958).
28. A. Okiji and J. Kanamori, Journal of the Physical Society of Japan, 19, 908 (1964).
29. C. Kittel, Quantum Theory of Solids, John Wiley & Sons, N. Y., 1966, Chapter 4.
30. V. K. Heine, Group Theory in Quantum Mechanics, Pergamon Press, Oxford (1964).
31. B. N. Brockhouse, Proceedings of the Symposium on Inelastic Scattering of Neutrons in Solids and Liquids, International Atomic Energy Agency, Vienna (1961), p. 113.
32. M. K. Wilkinson, H. G. Smith, W. C. Koehler, R. M. Nicklow, and R. M. Moon, in Neutron Inelastic Scattering, Vol. II, I.A.E.A., Vienna (1968), p. 253.
33. P. G. De Gennes, in Magnetism, 3, ed. G. T. Rado and H. Suhl, Academic Press, N. Y. (1963), p. 115.
34. W. M. Lomer and G. G. Low, in Thermal Neutron Scattering, ed. P. A. Egelstaff, Academic Press, London (1965), p. 1.
35. M. J. Cooper and R. Nathans, Acta Crystallographica, 14, 357 (1967).

36. M. J. Collins, V. Minkiewicz, and R. Nathans, BNL Report #12861.
37. I. Maartense, Physical Review, 188, 924 (1969).
38. J. S. Smart, Effective Field Theories of Magnetism, W. B. Saunders Co., Philadelphia and London (1966), p. 61.
39. J. P. Mahoney, C. C. Lin, W. H. Brumage, and F. Dorman, Journal of Chemical Physics, 53, 4286 (1970).
40. R. E. Watson and A. J. Freeman, Acta Crystallographica, 14, 27 (1961).
41. R. A. Cowley, W. J. L. Buyers, P. Martell, and R. W. H. Stevenson, Physical Review Letters, 23, 86 (1969).
42. T. M. Holden, E. C. Svensson, W. J. L. Buyers, R. A. Cowley, and R. W. H. Stevenson, Journal of Applied Physics, 41, 896 (1970).
43. E. R. Cowley and A. K. Pant, private communication.
44. P. R. Bevington, Data Reduction and Error Analysis for the Physical Sciences, McGraw-Hill, N. Y. (1969), Chapter 11.
45. W. R. Busing, private communication.
46. D. E. Wrege, in Papers and Presentations of the Digital Equipment Computer Users Society, Spring 1970, p. 77.
47. D. E. Wrege, FOCAL: How to Write New Subroutines and Use Internal Routines, DECUS Library, FOCAL-17, Maynard, Mass. (1969).
48. Small Computer Handbook, Digital Equipment Corp., Mass. (1967).
49. Logic Handbook, Digital Equipment Corp., Mass. (1968).
50. Introduction to Programming, Digital Equipment Corp., Mass. (1969), Chapter 9.

VITA

Douglas Ewart Wrege was born in Austin, Texas on November 11, 1943. He is the son of Edgar E. Wrege and Mildred N. Wrege.

He attended public schools in Lakeland, Florida and Swarthmore, Pennsylvania, and was graduated from Swarthmore High School in June, 1961. He entered the University of Rochester, Rochester, New York, in 1961, and graduated with a Bachelor of Science degree in Physics in 1965. He entered the Graduate Division of the Georgia Institute of Technology in September, 1965 and received the Master of Science degree in Physics in June, 1967. He is a member of Sigma Xi and other honorary societies.

In July, 1968, he was married to Julia Dallas Bouchelle, and they have one son, Dallas Ewart Wrege.